2009

Characterization of iron oxide thin films for photoelectrochemical hydrogen production

Kyle Eustace Nelson George
University of Nevada Las Vegas

CHARACTERIZATION OF Fe_2O_3 THIN FILMS FOR PHOTOELECTROCHEMICAL HYDROGEN PRODUCTION

by

Kyle Eustace Nelson George

Bachelor of Arts
University of Nevada, Las Vegas
2008

A thesis submitted in partial fulfillment
of the requirements for the

Master of Science in Chemistry Degree
Department of Chemistry
College of Sciences

Graduate College
University of Nevada, Las Vegas
December 2009

UNLV
UNIVERSITY OF NEVADA LAS VEGAS

THE GRADUATE COLLEGE

We recommend that the thesis prepared under our supervision by

Kyle Eustace Nelson George

entitled

Characterization of Fe_2O_3 Thin Films for Photoelectrochemical Hydrogen Production

be accepted in partial fulfillment of the requirements for the degree of

Master of Science
Chemistry

Clemens Heske, Committee Chair

David Hatchett, Committee Member

Dong-Chan Lee, Committee Member

James Selser, Graduate Faculty Representative

Ronald Smith, Ph. D., Vice President for Research and Graduate Studies
and Dean of the Graduate College

December 2009

ABSTRACT

Characterization of Fe_2O_3 Thin Films for Photoelectrochemical Hydrogen Production

by

Kyle Eustace Nelson George

Dr. Clemens Heske, Examination Committee Chair
Professor of Materials/Physical Chemistry
University of Nevada, Las Vegas

Solar energy is the most sustainable source of energy available. However, solar applications such as photovoltaic cells represent only a partial solution to weaning our dependence upon fossil fuels. Several methods of storing solar energy are currently being pursued, and chemical storage stands out as a promising option – combining design simplicity with high energy density, with hydrogen being particularly attractive because of its abundance and inherently clean nature. A monolithic Photoelectrochemical (PEC) device that produces hydrogen by electrolyzing water directly from sunlight has the benefit of utilizing "free" solar energy to drive the reaction.

Although α-Fe_2O_3 (hematite) is a strong candidate for PEC applications with a bandgap of 2.2 eV, its conduction band minimum is generally believed to be positioned below the H^+/H_2 reduction potential necessary for its use as a water splitting material. Additionally, the low charge carrier mobility of hematite implies that charge carrier recombination needs to be overcome. Despite this, α-Fe_2O_3 is cheap and abundant, nontoxic and easily synthesized. Furthermore, several studies have shown that this material is particularly receptive to both n- and p-type doping

– a solution that may address both the band edge position and charge mobility issues.

This thesis describes X-ray Photoelectron Spectroscopy (XPS) conducted at UNLV, Atomic Force Microscopy (AFM) imaging performed by Dr. Asanga Ranasinghe (also UNLV), Scanning Electron Microscopy (SEM) characterization by Arnold Forman and Alan Kleiman-Shwarsctein at the University of California, Santa Barbara (UCSB), and the synthesis process of α-Fe_2O_3 samples grown by our collaborators Arnold Forman, Alan Kleiman-Shwarsctein, and Dr. Eric McFarland at UCSB. We describe the synthesis process and report our observations of Ti diffusion through the Ti/Pt substrate interface and of Fe_2O_3 island growth due to high calcination temperatures. Furthermore, we identify contaminants incorporated into the samples, and correlate these findings with PEC sample performance.

ACKNOWLEDGEMENTS

Although thesis writing is formally an individual activity, this work would not be possible were it not for the amazing support I have had from advisors, colleagues, friends, and family along the way.

To my thesis committee: in the most literal sense I would be unable to produce this document without you, however my gratitude goes far beyond this. Professor James Selser, by giving me a strong foundation in basic physics, you have given me the tools to explore science and the world, leading me down a path that has brought us to this point. Professor Dong-Chan Lee, in academia your enthusiasm and good nature may be less important than the extent of your knowledge, but as a student, I believe your approachability has made your knowledge more accessible. I truly appreciate your feedback, advice and general conversation over the years. Professor David Hatchett, having taken several classes with you over the years, inviting you to serve on my committee was an easy decision, for I strongly associate my self-identity as a chemist with your training. I admire your ability to speak directly when the situation so requires, and I respect your protectiveness of those around you.

Professor Clemens Heske, I cannot fully express the depth of my appreciation for your mentorship and guidance through the years –academically, professionally and personally. As an undergraduate, you involved me in world-class research that many scientists can only dream of having access to. You opened the door to graduate school, and allowed me to arrive at the decision to walk through it – forever changing my life's path. More importantly, your council has helped me

through the toughest points in my personal life; supporting me when I needed support, encouraging me when I needed encouragement, and listening when I needed an ear. It is this personal attention that has won you the respect, admiration and devotion of your research group.

I also owe sincere thanks to Professor Eric McFarland of the University of California, Santa Barbara for providing the samples, resources and support that allowed me to conduct the research that developed into this thesis. His graduate students Arnold Forman and Alan Kleiman-Shwarsctein have spent countless hours assisting me throughout this process, and deserve more than passing thanks. You have been gracious and accommodating hosts, and I appreciate your sacrifice of weekends and late nights and too-early mornings. I value the friendship that has grown over the course of our working relationship.

To my friends and colleagues in Professor Heske's Research Group, your support through my ups and downs has allowed me to complete not only my undergraduate degree, but my Master of Science degree. Never have I been part of a working environment with such complete and total support for fellow colleagues. At times of great personal trials, you have shouldered some of my workload so I could focus on these issues, and this willingness to help out did not go unnoticed, or unappreciated. The post-doctoral scholars who have passed through our group have set the standard for excellence by the breadth of their knowledge and experience. Dr. Lothar Weinhardt, Dr. Marcus Bär, Dr. Yufeng Zhang, Dr. Ich Tran, Dr. Asanga Ranasinghe, and Dr. Stefan Krause, I admire your expertise and strive to attain your level. I extend special thanks to Dr. Zhang for reviewing my early drafts,

to Dr. Ranasinghe for the AFM imaging that helped me better understand my data. I especially thank Dr. Krause for being my coffee partner, for spending hours discussing my experimental design over many cups of coffee, and for reining me in when my plans exceeded my schedule and capabilities.

To my fellow graduate students, Moni Blum, Timo Hofmann, and Sujitra Pookpanratana, who have shown me how a raw graduate student develops into a Ph.D. Watching you blaze the trail has shown me that although the road may be long, it is certainly surmountable. Thank you for all your support and help. Thanks also go out to the undergraduates in our research group, Doug Hanks, Graham Haugh, Fatima Khan, and Bhakthi Amarasinghe.

To my friends who have supported me throughout my entire academic career, you have sometimes had more confidence in me than I have had in myself, and for this I thank you.

And finally, I dedicate my thesis to my family. To my mom, Marjorie Reyes, and to my dad, Nelson George, both of whom have always placed education above all else. To my own new family: Dr. Sarah Johnson, who sacrificed alongside me when I chose to return to academia, and stood by my side throughout it all. Thank you for having the faith in me that allows me to keep going; thank you for your love; and thank you for the greatest gift in my life. To our daughter, Mackenzie Elizabeth George, you may not have understood why daddy did not give you all the time and attention you deserved over the last few months, yet you always forgave me, and that means the world to me. Your daddy loves you more than you will ever know, and I work every day hoping to become the role model you can look up to.

TABLE OF CONTENTS

LIST OF FIGURES

LIST OF ABBREVIATIONS

α-Fe_2O_3 ..... Alpha phase iron oxide (hematite)
Ar ..... Argon
Cr ..... Chromium
F ..... Faraday's Constant
Fe2O3 ..... Iron oxide
I_p ..... Photocurrent density
IMFP ..... Inelastic Mean Free Path
IPCE ..... Incident Photon-to-Current Efficiency
λ ..... Wavelength (Lambda)
N_2 ..... Molecular nitrogen
O_2 ..... Molecular oxygen
PEC ..... Photoelectrochemical
PES ..... Photoelectron Spectroscopy
Φ ..... Work function (Phi)
Pt ..... Platinum
S_c ..... Solar constant
SEM ..... Scanning Electron Microscope
SIMS ..... Secondary Ion Mass Spectroscopy
Ti ..... Titanium
TiO_2 ..... Titanium dioxide
UCSB ..... University of California, Santa Barbara
UHV ..... Ultra-high vacuum
UNLV ..... University of Nevada, Las Vegas
XPS ..... X-ray Photoelectron Spectroscopy

CHAPTER 1

INTRODUCTION

1.1 Background and Motivation

The concept of alternatives to fossil-based fuels is attractive for many reasons. Strictly speaking, "alternative energy" simply means energy from sources other than that which have been traditionally used. More colloquially, "alternative energy" refers to energy sources that are sustainable, renewable and minimally impact the environment. "Sustainability" refers to the ability to meet demand and continue to serve as an energy source far into the future, whereas "renewable" means that its use does not diminish its overall supply, or that its quantity regenerates over time. For this reason, although nuclear power may be considered a clean, sustainable energy source, it fails the renewability criteria and is not considered an alternative energy in the sense with which we will be using the term.

All alternative energy solutions have their advantages, but they also come with accompanying drawbacks, and no one solution is globally utilizable. An alternative energy culture will ultimately be one that balances several technologies and multiple philosophies. In the end, the choice of a "best" alternative energy solution will depend on several rubrics and vary widely by location.

1.1.1 Solar Energy

Because life on earth is entirely dependent upon our sun, solar energy is the most sustainable energy source available. The sun's energy output is vast, and its total electromagnetic radiation energy density (defined as the "solar constant" (S_c))

has been quantitatively measured as 1366.1 Wm^{-2} [1]. It is important to note that the sun's output is not constant, and may vary with solar activity and for that reason the solar constant can be may be more formally calculated with:

$$S_C = \int_0^\infty E_\lambda d_\lambda \qquad \textbf{(Equation 1-1)}\ [1]$$

where E_λ is the sun's spectral irradiance. Just outside the earth's atmosphere the Inverse Square Law applies and can be used to quantify the energy as:

$$I = E_\lambda \frac{4\pi R^2}{4\pi r^2} \qquad \textbf{(Equation 1-2)}$$

However, since solar energy is attenuated by the atmosphere and is strongly dependent upon the angle of the incoming sunlight, the solar constant does not apply to terrestrial applications. On Earth, insolation is a more relevant measurement of the energy that hits its surface, and is calculated as follows [2]:

$$I = S\cos Z \qquad \textbf{(Equation 1-3)}$$

where

$$S \cong 1000\, Wm^{-2} \qquad \textbf{(Equation 1-4)}$$

and

$$Z = cos^{-1}(sin(\Phi)\, sin(\delta) + cos(\Phi)\, cos(\delta)\, cos\,(H)) \qquad \textbf{(Equation 1-5)}$$

In the above equations, Φ is defined as the latitude, δ is the solar declination angle and *H* is the "Hour angle". The solar declination angle accounts for seasonal changes in the sun's angle as the earth orbits the sun, whereas the hour angle accounts for the angle of radiation due to the sun as a function of time, and is calculated as:

$$H = 15^{\circ}(Time - 12) \qquad \textbf{(Equation 1-6)}$$

When insolation is integrated across time and plotted with the solar constant as a function of wavelength, we get the "Standard Solar Spectrum" (ASTM G-173-03) reference plot that is used to model solar applications. This chart assumes a solar zenith angle of 48.19° that corresponds to an average of the latitudes that span the North American continent.

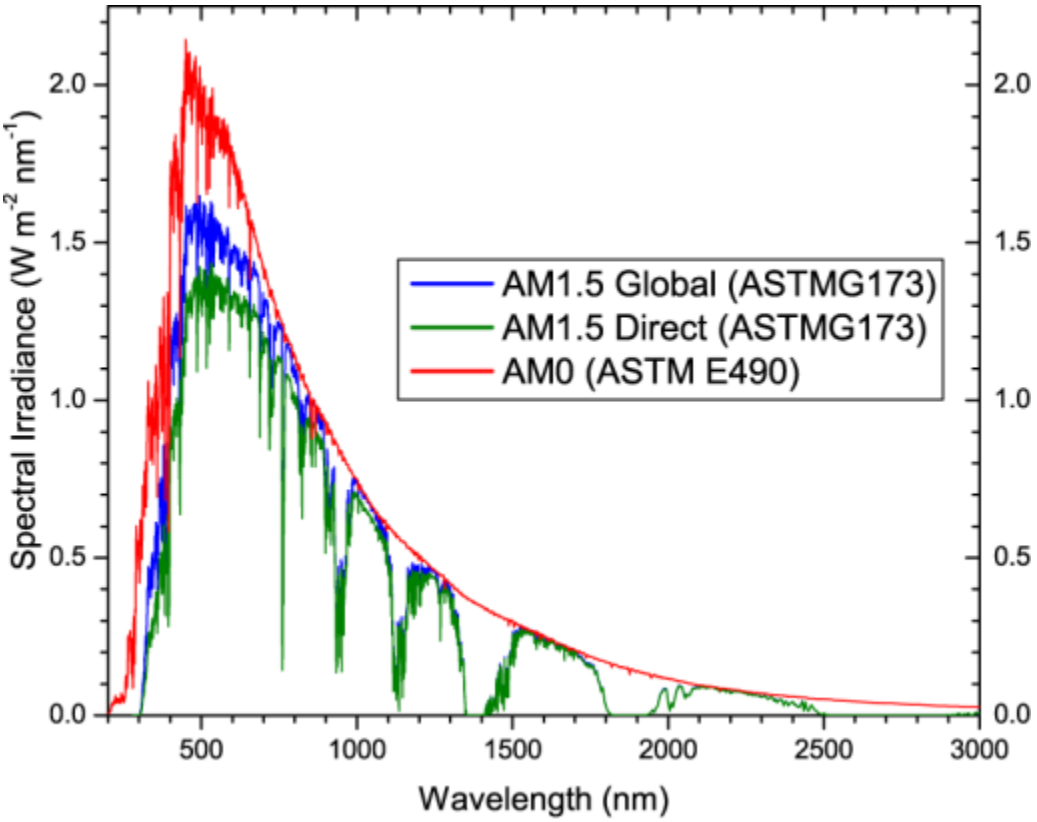

Figure 1.1: Standard Solar Spectra for space and terrestrial use [3].

AM1.5 in Figure 1.1 (above) adjusts insolation for atmospheric attenuation and is done by factoring in several components, including turbidity, water vapor content, ozone, and atmospheric absorption properties as defined by the National Oceanic

and Atmospheric Administration in "U.S. Standard Atmosphere, 1976" [4]. Because this model assumes 48° zenith angle, the solar energy path through the atmosphere becomes *cos*(48°), hence approximately 1.5 atmospheres of attenuation. In practice, the AM1.5 Global spectrum is used for flat plate solar applications, whereas the AM1.5 Direct spectrum is used for solar concentrator applications [3]. The integration of the AM1.5 Global and AM1.5 Direct spectra give us 1000 Wm^{-2} and 900 Wm^{-2} respectively. AM0 applies to solar activity outside the earth's atmosphere and may be considered a plot of the solar constant by wavelength or the Inverse Square Law.

With such high terrestrial energy density, solar energy is capable of meeting the earth's power demands; however, it must be stored in some manner if it is to be used as a reliably consistent source of energy.

1.1.2 Hydrogen

Chemical storage of energy involves using the energy to assist the formation of thermodynamically unfavorable bonds, then breaking these bonds and capturing the excess energy. Of the chemical forms to store energy, hydrogen is particularly attractive because of its abundance and inherently clean nature. Whether used in a fuel cell, or directly combusted, the only byproduct of hydrogen energy is water. Hydrogen is often included in discussions of alternative energy, but should be more properly described as an energy carrier rather than an energy source [5] – except in the case of hydrogen fusion. What makes hydrogen unique among the alternative energy methods previously discussed, however, is its promise for transportation applications. Although all of the above solutions help diversify our energy

composition, few of them apply towards transportation, unless sufficient advances in battery technology can be made.

Hydrogen is an attractive energy carrier because it can be efficiently converted into a usable form such as electricity (with a theoretical maximum efficiency of 83% [6]), and yet is versatile enough to be used directly as a fuel in combustion engines.

To compare, the Carnot limit of a steam turbine at 400°C and a heat sink at 50°C produces a theoretical maximum efficiency of 52%. Real world efficiency numbers for internal combustion gasoline engines range between 30% - 40% [7], with most of the gasoline's energy lost as waste heat. Diesel engines achieve higher fuel conversion efficiencies, but still less than that of hydrogen. Currently, efficiencies of commercial fuel cell systems are observed to reach 60% [8]. The latest designs allow coal power plants to reach up to 45% efficiency [9].

The production of hydrogen is only one factor to be considered. Even if hydrogen can be produced cheaply and efficiently, there are still practical limitations about how it will be transported to the end user, how it will be stored, and how it will be consumed. Although extremely important when evaluating hydrogen, these questions are outside the scope of this thesis, and we will restrict our discussion to its production via photoelectrochemical water splitting.

CHAPTER 2

PHOTOELECTROCHEMICAL WATER SPLITTING

2.1 Background and Motivation

Since Fujishima and Honda first proposed direct sunlight "water splitting" in 1972 [10], much research has been invested into finding suitable materials for use as photoelectrodes. Electrolyzers can accomplish water splitting without the requirement for sunlight, but the ohmic resistance of the circuitry and electrolytes [11] contribute inefficiencies to the system, making electrolyzers an expensive method of hydrogen production. A monolithic device that electrolyzes water directly from sunlight has the benefit of skipping this intermediate step and directly utilizing "free" solar energy to drive the reaction, and thus presents the possibility of synergy to reduce the energy requirements.

For a material to be suitable for photoelectrochemical (PEC) water splitting, it must simultaneously satisfy several requirements. Candidates must be durable under harsh electrolytic environments ranging from pH 14 to pH -1 and have an electronic bandgap larger than 1.23 eV. Both the photosensitive working electrode, and its counter electrode must be optimized with respect to the oxidation and reduction potentials of H_2O. Overcoming overpotential losses require a minimum of 1.6 eV to 1.8 eV, but a comparison to commercial electrolyzers shows that a band gap of 1.9 eV is more realistic for water splitting in this type of device [12].

PEC materials must not only have the proper band edge alignment, they must also have the right optical bandgap, absorbing in the visible light spectrum.

Quantitatively, we can calculate the optimal absorption required with the following equation:

$$E = \frac{hc}{\lambda} \qquad \textbf{(Equation 2-1)}$$

where *h* is Planck's Constant, and *c* is the speed of light. Solving for λ, and assuming E=1.9 eV, the ideal PEC material requires absorption at approximately 650 nm and below, corresponding to region of the solar spectrum with the highest flux as seen in Figure 1.1.

2.1.1 Fe_2O_3 Photoanodes

Figure 2.1 shows a diagram of an Fe_2O_3 photoelectrochemical cell.

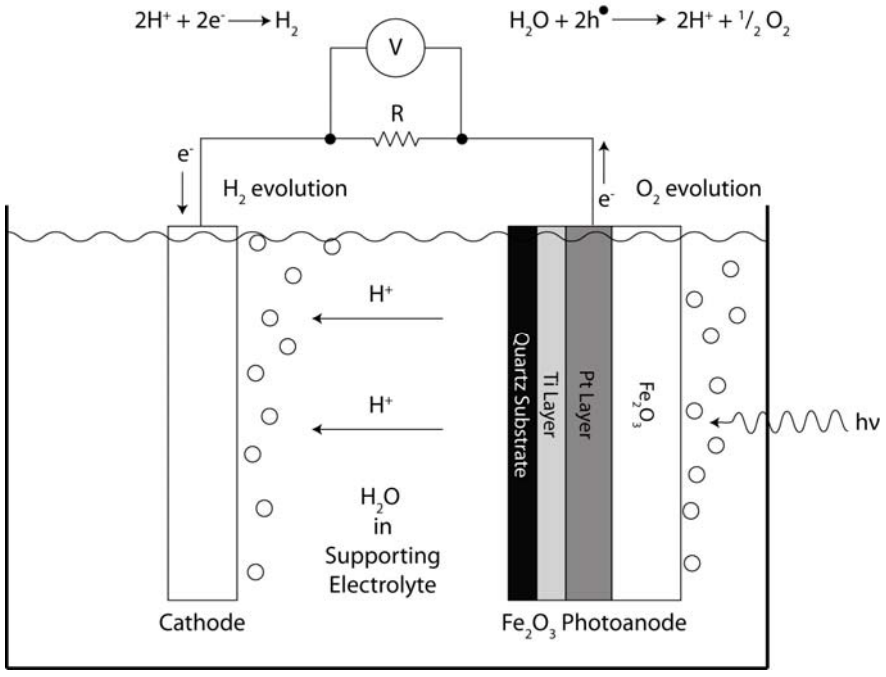

Figure 2.1: Diagram of Fe_2O_3 Photoelectrochemical Cell (based on [13]).

The photoelectric water splitting process begins with photonic excitation of the photosensitive Fe_2O_3 film. This process occurs when the energy of two incoming photons is sufficiently high to promote two electrons from the valence band to the conduction band. This process is described in Equation 2-2,

$$Fe_2O_3 + 2h\upsilon \rightarrow 2e^- + 2h^\bullet \qquad \textbf{(Equation 2-2)}$$

where e^- represents an electron, and $h^\bullet$ represents a (positively charged) hole. At the anode, the water is oxidized and evolves atomic oxygen at the site.

$$2h^\bullet + H_2O \rightarrow \tfrac{1}{2}O_2 + 2H^+ \qquad \textbf{(Equation 2-3)}$$

The positively charged H^+ cations move through the electrolyte towards the cathode, and reduce to molecular hydrogen at the site:

$$2e^- + 2H^+ \rightarrow H_2 \qquad \textbf{(Equation 2-4)}$$

The overall reaction for the cell is thus:

$$H_2O + 2h\upsilon \rightarrow \tfrac{1}{2}O_2 + H_2 \qquad \textbf{(Equation 2-5)}$$

Since both oxidation and reduction occur in the photoelectrochemical water splitting process, a PEC material must have a bandgap that straddles both the oxidation and reduction potentials of H_2O (a necessary, but not sufficient condition). Additionally, the best cells should absorb the region of the solar spectrum with the most available number of photons (intensity) – therefore in the visible portion of the spectrum, and particularly around 600 nm, as discussed in Section 2.1.

The need for electrolytes to support photocatalytic water splitting further complicates the materials science challenge of developing high-performing PEC devices. The electrolyte facilitates ionic transport through the system and lowers the overall resistance of the circuit. A properly chosen electrolyte can shift the

bandgap position to better straddle the oxidation/reduction potentials. However, this comes at the cost of a corrosive environment, with conditions ranging from pH -1 to 14. Finding materials that are stable under these conditions, while simultaneously satisfying the band position and gap requirements is greatly challenging, and much of the focus of PEC research is directed towards the search for suitable candidate materials.

Because of its high durability in electrolyte and its favorable bandgap of 2.2 eV, α-Fe_2O_3 (hematite) is a strong candidate for PEC applications [14]. α-Fe_2O_3 is cheap and abundant, nontoxic and easily synthesized, and it absorbs at approximately 650 nm and below. Its 2.2 eV bandgap is slightly too large for efficient water splitting, but within acceptable limits. However, its conduction band minimum is thought to be positioned below the H^+/H_2 reduction potential necessary for water splitting [15]. It is thus necessary to adjust the band edge positions, e.g., by doping or hybridization. Several studies have shown that iron oxide is particularly receptive to both n- and p-type doping [16].

A more difficult challenge to overcome is the low charge carrier mobility of Fe_2O_3. Iordanova, Dupuis, and Rosso describe how electrons in pure hematite must first overcome an activation barrier before hopping can occur, and even then are limited to movement along the (001) plane [17]. This inability to efficiently transfer charge means that recombination rates are high, and the net current low. Like the bandgap issue, strategic doping may provide the solution to this problem.

To facilitate the movement of charge, two doping approaches can help to optimize the performance of a PEC-type device. N-type doping is done by

introducing pentavalent (Group V) atoms into the lattice, shifting the Fermi level upwards. Common n-type dopants are phosphorus (P), arsenic (As), or antimony (Sb), and because these pentavalent atoms have one extra electron in the valence shell, they are excellent electron-donors, shifting the Fermi level towards the conduction band. P-type doping is usually done with trivalent (Group III) atoms such as boron (B), aluminum (Al) or gallium (Ga), where the reduced number of electrons in the valence shell creates a hole, such that these elements function as electron-acceptors, and shift the Fermi level closer to the valence band.

Another promising approach is to employ nanostructured materials. By approaching the nanoscale, materials are subject to quantum confinement effects – allowing bandgap engineering by modifying the size and shape parameters.

For these reasons, studies of the electronic properties of α-Fe_2O_3 and possibilities to tailor them for optimal use in PEC applications continue to be of interest to the alternative energy research community. The Fe_2O_3 films discussed in this thesis were synthesized by Alan Kleiman-Shwarsctein, Arnold Forman, and Eric McFarland at the University of California, Santa Barbara, using electron-beam deposition and subsequent calcination. A more detailed description of the sample preparation process will be presented in Chapter 4.

CHAPTER 3

EXPERIMENTAL TECHNIQUES & INSTRUMENTS

3.1 X-ray Photoelectron Spectroscopy

3.1.1 Photoelectron Spectroscopy Overview

Photoelectron Spectroscopy (PES) is a class of photon-in, electron-out spectroscopic techniques that is rooted in the external photoelectric effect first recognized by Hertz in 1887 [18], and further described and expanded by Hallwachs in 1888 [19]. In 1905 Einstein advanced the theory by proposing that light was quantized, with the energy of each quantized unit or photon being a function of its frequency and a constant. For this discovery, Einstein won the 1921 Nobel Prize in Physics.

The photoelectric effect states that when a solid is excited by a photon with an energy above a certain threshold, it absorbs this energy and emits an electron to a point where the electron no longer feels the influence of the solid. This threshold is related to the binding energy (E_{bin}) of the electron, and the point at which the surface-electron interactions are minimal is called the vacuum level. The work function (Φ) of the solid is the energetic distance between its Fermi Energy (E_F) and the vacuum level. The kinetic energy of this ejected electron can thus be mathematically described as

$$E_{kin} = h\upsilon - E_{bin} - \Phi. \qquad \textbf{(Equation 3-1)}$$

PES utilizes the photoelectric phenomenon by irradiating a sample of interest with photons of known energy. An electron analyzer measures the kinetic energy

and number of the electrons leaving the sample's surface with an electron analyzer. Preserving the energy of these electrons requires a relatively unobstructed path to the analyzer – necessitating ultra-high vacuum (UHV) conditions for PES. UHV has the added benefit of minimizing sample surface contamination, which is extremely important due to the surface sensitivity of these techniques.

3.1.2 Inelastic Mean Free Path

The surface sensitivity of PES, and the need for ultra-high vacuum conditions is best described by the Inelastic Mean Free Path (IMFP), λ. The "Universal Curve" in Figure 3.1 below shows an approximate relationship between the kinetic energy of an electron and its IMFP.

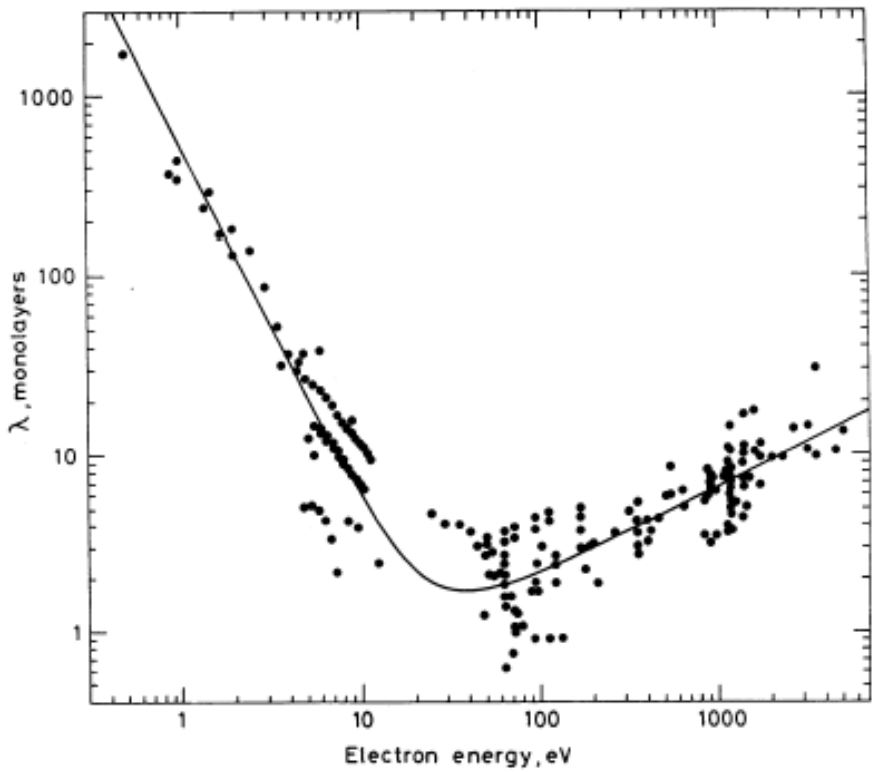

Figure 3.1: The Universal Curve of IMFP in solids [20].

As seen in this figure, the most surface-sensitive situation occurs for a kinetic energy of approximately 30 eV. For kinetic energies lower than 30 eV, λ decays by $E_{kin}^{-0.5}$, whereas at energies above 30 eV, the behavior is approximately $E_{kin}^{0.5}$. Depending on $h\nu$, photons may penetrate a sample at depths up to μm, but with the energy range used in PES techniques, only electrons within the first few nm of the solid will have an inelastic-collision-free path out of the solid. For this reason, PES techniques are extremely surface-sensitive and limited to an information depth of approximately 10 nm.

This sensitivity also motivates the need to preserve a sample's surface. Collision flux in air occurs at

$$Z_W = \frac{Z_0\left(\frac{p}{Pa}\right)}{\left\{\left(\frac{T}{K}\right)\left(\frac{M}{g\ mol^{-1}}\right)\right\}^{\frac{1}{2}}}. \qquad \text{(Equation 3-2)}$$

At room temperature in ambient pressure, each atom on the surface is hit by other atoms approximately 10^8 times per second, effectively covering the sample and rendering it useless for PES. By moving to pressures of 10^{-9} Pa, the collision flux decreases to approximately one time every 10^6 seconds [21].

3.1.3 Heske Group's XPS Capabilities

X-ray Photoelectron Spectroscopy (XPS) is differentiated from other PES techniques by the energy of the photons used. The UNLV Heske Lab uses both Mg K_α (1253.6 eV) and Al K_α (1486.6 eV) X-ray sources for XPS experiments performed on site. The lab contains two XPS systems - The "Andere ESCA" and the VG SCIENTA sytems.

The Andere ESCA possesses a high flux Specs XR50 twin-anode X-ray source and a Specs Phoibos 150MCD concentric hemispheric analyzer with a 9-channel electron multiplier. The X-ray source has the capability to provide both Mg K_α and Al K_α X-ray characteristic radiation with a line width of 0.7 eV and 0.85 eV respectively [20]. Figure 3.2 shows a schematic diagram of the experimental setup for X-ray Photoelectron Spectroscopy. For a more detailed discussion of the XPS experimental technique, refer to Surface Analysis: The Principal Techniques, by Briggs and Seah [20].

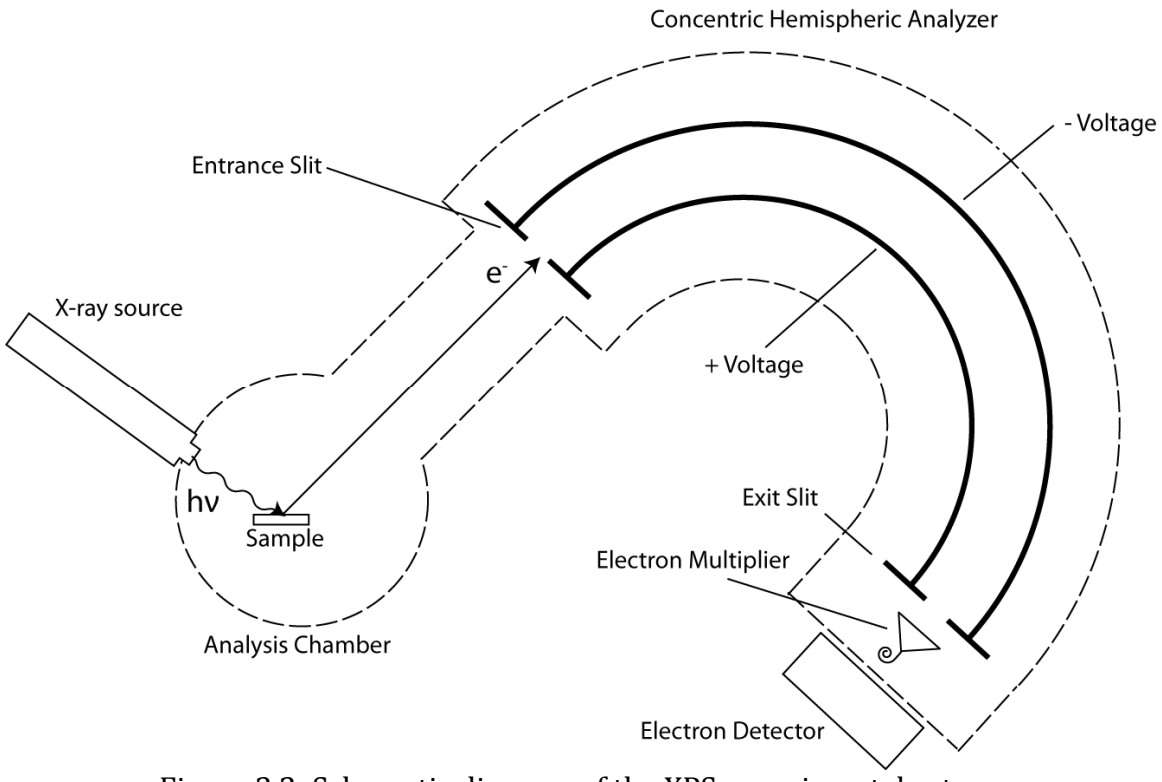

Figure 3.2: Schematic diagram of the XPS experimental setup.

The Heske group also utilizes a VG Scienta R4000, 200 mm radius spectrometer in concert with an MX650 x-ray source package. This package combines the SAX100 Al K_α X-ray source with an XM-780 X-ray monochromator, resulting in a high intensity light with a resolution better than 0.3 eV. This system has the additional benefit of reduced background and no satellite lines in its XPS spectra. The Scienta differs from the setup shown in Figure 3.2 primarily in the need for the X-rays to be monochromatized before reaching the sample. The means by which this is done (dispersive crystals) is illustrated in Figure 3.3 below.

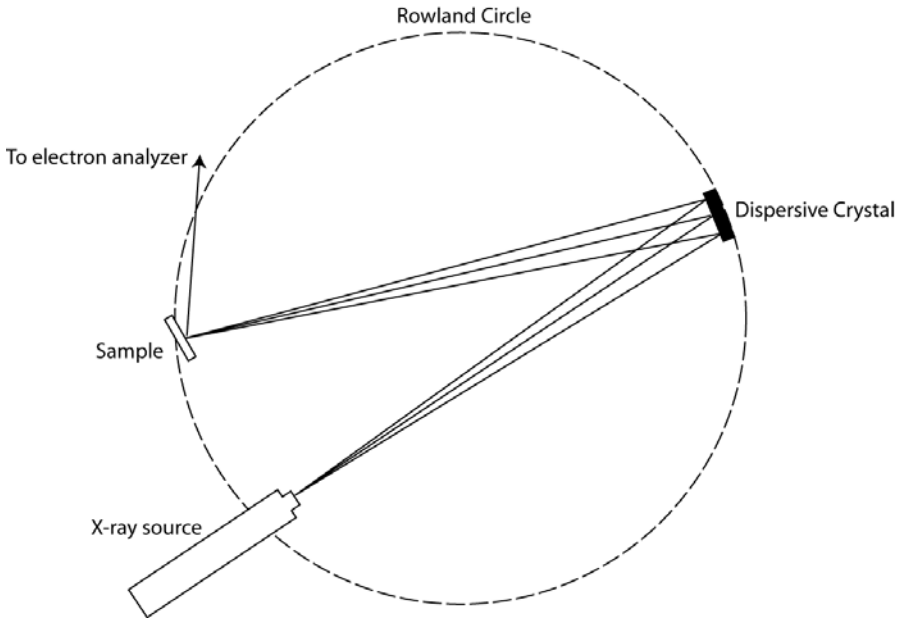

Figure 3.3: Monochromator operating principle.

Both systems described were used to collect XPS data discussed in this thesis. The characteristic spectra from XPS are shown and discussed in Chapter 5 – Results and Discussion.

3.2 Incident Photon-to-Current Efficiency

Incident Photon-to-Current Efficiency (IPCE) is an electrochemical experiment designed to measure the external quantum efficiency of photoelectrochemical cells, and is used in the PEC community to quantitatively evaluate a cell's performance as a water splitting device. IPCE tests are performed in either 2-electrode or 3-electrode systems, where the PEC material of interest is the working electrode. This electrode is placed in supporting electrolyte and illuminated with incident photons of varying wavelengths from a calibrated light source with known flux. The resulting current is measured and used to determine the IPCE as follows:

$$IPCE = \frac{I_P(\lambda)}{eF(\lambda)}, \qquad \textbf{(Equation 3-3)}[22]$$

where $I_p(\lambda)$ is the photocurrent density at a given wavelength and F is Faraday's Constant.

IPCE data presented in this thesis were collected by Arnold Forman and Alan Kleiman-Shwarsctein under Prof. Eric McFarland at the University of California, Santa Barbara. Further information about IPCE may be found on the Department of Energy's Photoelectrochemical Research Standards and Methods Development web page [23].

3.3 Atomic Force Microscopy

The Atomic Force Microscope (AFM) images shown in this thesis were taken by Dr. Asanga Ranasinghe of the Heske Group on a Park Systems XE-70. The XE-70 is

an Air-AFM with decoupled XY and Z scanners, which minimizes artifacts due to cross-talk [24]. As shown in Figure 3.4, an AFM operates by use of a cantilever tip in contact with the surface of the sample, and for this reason is extremely sensitive to surface topology. A laser beam is reflected off the end of the cantilever of known stiffness unto an array of photosensors, which measure the amount of deflection of the cantilever. An application of Hooke's Law then allows for determination of the deflective force by the formula

$$F = -kz\,, \qquad \textbf{(Equation 3-4)}$$

where k is the spring constant or stiffness of the cantilever and z is the amount of travel along the z-axis. As the probe tip rasters across the surface of the sample, these deflective forces are interpreted by imaging software to form an image of the topology. AFM microscopy is limited in resolution to the size of the probe tip (i.e., down to atomic resolution), and the maximally attainable length scale for a larger overview of the sample's surface is limited by the x-y scanner (50 μm^2 in our case).

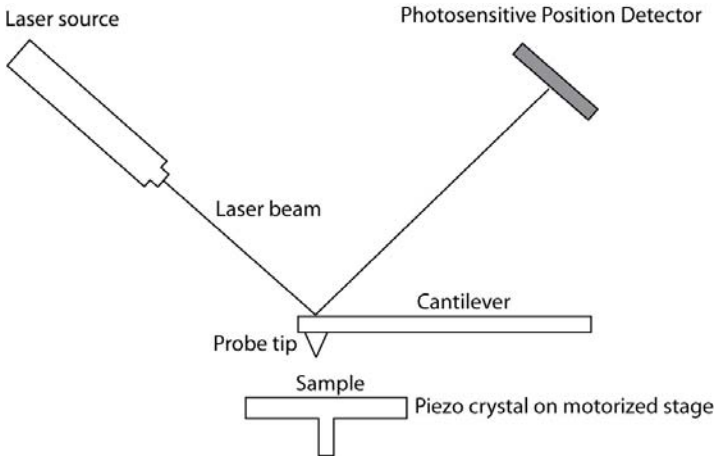

Figure 3.4: Simplified diagram of an Atomic Force Microscope.

3.4 Scanning Electron Microscopy

The Scanning Electron Microscope (SEM) is a non-contact microscopy technique that scans the surface of a sample with a narrow, highly-collimated beam of high-energy electrons. Interaction between this beam and the sample's surface cause secondary electrons due to inelastic scattering, which are then detected by an electron detector (due to this secondary electron emission mechanism, this technique is also sometimes referred to as Secondary Electron Microscopy). The resulting image is remarkably three-dimensional which, when used in conjunction with AFM images, was instrumental in characterizing the morphology of the α-Fe_2O_3 films in the present thesis. The SEM technique also allows for cross-sectional images to be taken. The images presented in this thesis were taken with an unspecified SEM microscope, and are courtesy of Arnold Forman and Alan Kleiman-Shwarsctein at UCSB.

CHAPTER 4

α-Fe_2O_3 THIN FILM SAMPLES

4.1 Introduction

Within the framework of the U.S. Department of Energy PEC Working Group, the McFarland Group at the University of California, Santa Barbara (UCSB), has been tasked with optimizing iron oxide thin films for PEC applications. All data presented in this thesis were taken on samples prepared by the UCSB group. The performance of these samples is determined by catalytic surface processes, and due to the surface-sensitive investigation techniques available to the Heske Group at the University of Nevada, Las Vegas, UNLV was charged with identifying systematic deviations that explain performance differences. This project was assigned to the author of this work, as the basis for his Master's Thesis research.

The scope of this project included development of a communication channel between UCSB and UNLV in order to provide inside-based optimization feedback on the sample growth processes, and establishment of a detailed understanding of the status quo baseline process by a thorough XPS investigation of prototypical samples. To gain an understanding of the production process, the author visited and participated in the growth of a batch of control samples as described in the next section. To avoid any contamination during shipping or transfer during production, the author introduced UNLV's clean N_2 glovebag sample handling approach, whereby samples are transferred from the production location to the analysis systems in an air-free environment.

The optimization of the samples required an understanding of several issues. First, it was previously observed that samples calcined in different ovens during the synthesis process produced different Incident Photon-to-Current Efficiency (IPCE) results in otherwise identical samples. Second, UCSB had produced one batch of samples that had outperformed any previously produced, but, with no obvious explanation for the performance differences, have been unable to reproduce the result. Secondary Ion Mass Spectrometry (SIMS) on other batches suggested contamination of Al and Cr in the Pt layer of the sample, but this had not been confirmed by other techniques. Lastly, UCSB asked for insights into the Fe/Pt interface of their Fe_2O_3 films.

4.2 Synthesis

The UCSB Fe_2O_3 samples were grown by e-beam deposition at the UCSB Nanofabrication Facility's Class 1000 (ISO 6) cleanroom. SiO_2 substrate wafers (4-inch diameter) were prepared for thin film deposition by O_2-etching on a Technics PE-IIA plasma etching system. The oxidized wafers were transported in air to the UCSB Vacuum Deposition E-Beam #4, a CHA Industries SEC600 Multi-Wafer Evaporator, where 50 nm of Ti was deposited via e-beam deposition at 2.4×10^{-6} Torr. This evaporator contains a gun-turret style carousel that stores several metals in carbon crucibles, rotating to the specific metal as needed. UCSB E-Beam #4 is also used to deposit Al, Ti, Au, Pt, Ni, Pd, Ag, Ge, and Cr.

After deposition, the Ti-covered wafers were sectioned in air, then moved to UCSB E-Beam #1, a Sharon Vacuum Four Pocket Electron Beam Evaporator. This evaporator is reserved for the evaporation of high purity metals, and was used to

deposit 150 nm of Pt and Fe layers of varying thickness. These depositions were done at a base pressure of 3.7×10^{-6} Torr.

To prevent exposure to air, the bell jar evaporator was outfitted with a plastic foil collar, attached to a glovebag, and sealed with adhesive tape. A FoodSaver® brand vacuum sealer, gloves, sample cases, and cleaned tools were placed in the glovebag, and vacuum lines and N_2 lines were attached to the gas inlet nipples of the bag. The bag was purged with N_2, evacuating the gas with the vacuum line, and refilling it with N_2. This cycle was repeated several times. After completion of the deposition process, the samples were removed under N_2 environment, placed in Fluoroware sample cases which prevent the surface from touching the container, and vacuum sealed with FoodSaver® bags. These bags were then placed within another bag filled with desiccant, and again vacuum-sealed.

The doubly sealed bags were transported from the UCSB Nanofab facility to a McFarland Group laboratory, placed in a glovebag (purged as described above), and removed from their bags under nitrogen to be cut into smaller pieces. These pieces were placed in a Lindberg/Blue tube furnace into which a metered mix of 80%/20% high purity N_2 and O_2 was streamed. An air trap was placed on the "far" side of the furnace tube to prevent air from entering the tube from the non-metered end. The May 2009 samples were calcined at 700°C for 8 hours, with a 2°C per minute ramp up to the calcination temperature. Earlier samples were calcined at 700°C for 4 hours, also with a 2°C per minute ramp. At the end of the calcination process, the furnace was turned off, with no controlled ramp-down of temperature. UCSB Scanning Electron Microscope (SEM) analysis showed that the post-calcination

Fe_2O_3 layer has approximately twice the thickness of the originally deposited Fe film.

After annealing, samples were allowed to cool down and again placed in Fluoroware sample holders, vacuum sealed, sealed again in a second bag with desiccant, and transported to UNLV. At UNLV, the bags were opened under N_2 environment in a glove-box and moved into ultra-high vacuum for XPS analysis without air exposure. At UNLV, samples were mounted to their holders with UHV-compatible carbon tape, and an Ohmic contact with the top surface was made by contacting a small metal clip of tantalum to a corner of the sample surface. The presence of an Ohmic contact was verified by checking for continuity between a distant corner of the sample surface and the base of the sample holder stub. The air-free packing procedure is shown below in Figure 4.1 and Figure 4.2.

Figure 4.1: N_2 glovebag sample extraction setup.

Figure 4.2: Furnace 1 glovebag setup.

4.3 Experimentation

Because of the extended periods of x-ray radiation to which samples are being subjected in XPS experiments, a study focusing on the potential presence of beam-induced modifications was conducted. To this end, a series of fast scans of the Fe 2p and O 1s XPS peaks of a sample with (nominal) Fe-film thickness of 475 nm was performed. Three fast scans of these peaks were taken before standard survey and detailed scans were collected. Additional fast scans of the Fe 2p and O 1s peaks were taken intermittently during and after sample analysis, for a total of ten scans. As will be discussed in Chapter 5, these scans show no spectroscopic evidence of beam-induced damage.

XPS survey scans were taken of all samples, followed by detailed scans of areas of interest. XPS scans from different samples were examined and compared against each other to identify common features, as well as meaningful differences. The chemical composition of elements in the samples was quantified, and these data were then correlated to UCSB data on sample performance and used to develop models explaining sample composition and its effect on performance.

The effect of the calcination step on the Ti/Pt interface was also examined. An unheated sandwich sample, consisting of 150 nm of Pt on top of 50 nm of Ti on the quartz substrate, was examined with a monochromatized Al K_α x-ray source in the VG SCIENTA XPS system at UNLV. A baseline spectrum was recorded, followed by iterative measurements after discrete periods of heating the sample on the sample holder stage. Another sample was annealed in air in UNLV's Lindberg/Blue M furnace at 700°C for four hours, and then also examined by XPS in the VG SCIENTA system. These spectra were then analyzed to develop a model for the effect of calcination on the Ti/Pt interface.

The morphology of the sample surfaces was imaged in air with a PSIA XE-70 E non-contact Atomic Force Microscope (AFM) by Dr. Asanga Ranasinghe. Images were taken of annealed and unannealed Fe-coated samples, as well as annealed and unannealed Pt surfaces. Images of the anomalous, outperforming "mystery" sample were also collected and examined.

The results of these experiments are presented and discussed in Chapter 5 of this thesis.

CHAPTER 5

RESULTS AND DISCUSSION

5.1 Sample and Experimental Quality Control

Figure 5.1 shows a typical XPS survey scan of a reference Pt spectrum.

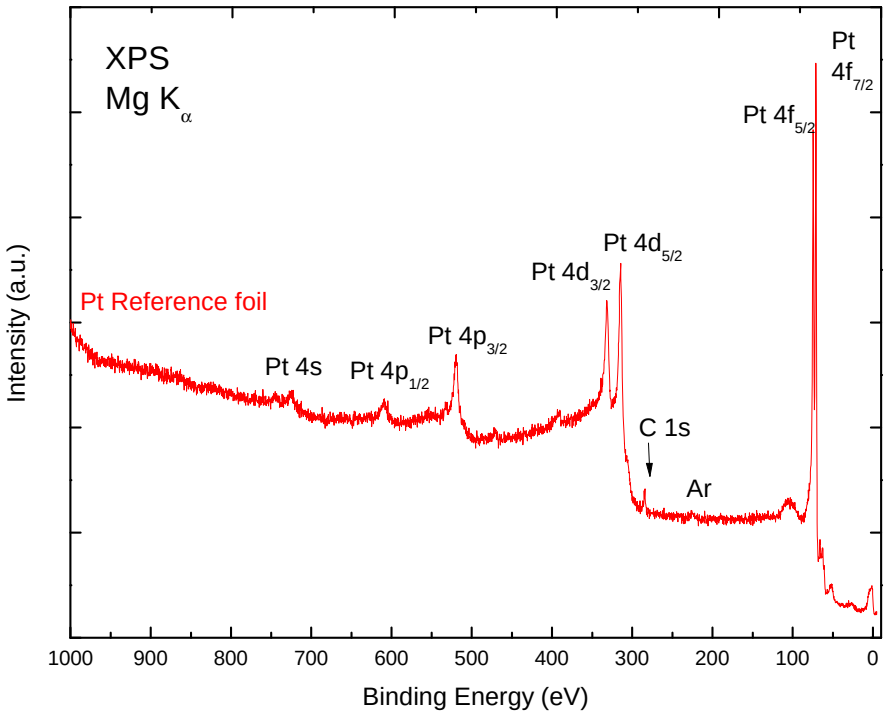

Figure 5.1: XPS spectrum of a reference Pt foil.

The shape and position of the peaks give a detailed view of the surface that is element-specific and highly instructive about the chemical environment. Line positions of reference metals can also be used to calibrate the XPS system, and by

comparing the binding energy position Pt $4f_{7/2}$ peak of a sputtered Pt foil surface in Figure 5.1 against that of a reference Pt spectrum [25], we were able to verify the energy axis alignment of our XPS system and all presented spectra.

Because x-ray irradiation has been shown to be destructive to some materials [26,27], it was first necessary to determine the impact of x-rays on the sample surface and, in particular, its electronic and chemical structure. Beam damage studies were conducted by recording baseline spectra of the O 1s and Fe 2p peaks, and then observing changes to the spectra after extended exposure to radiation.

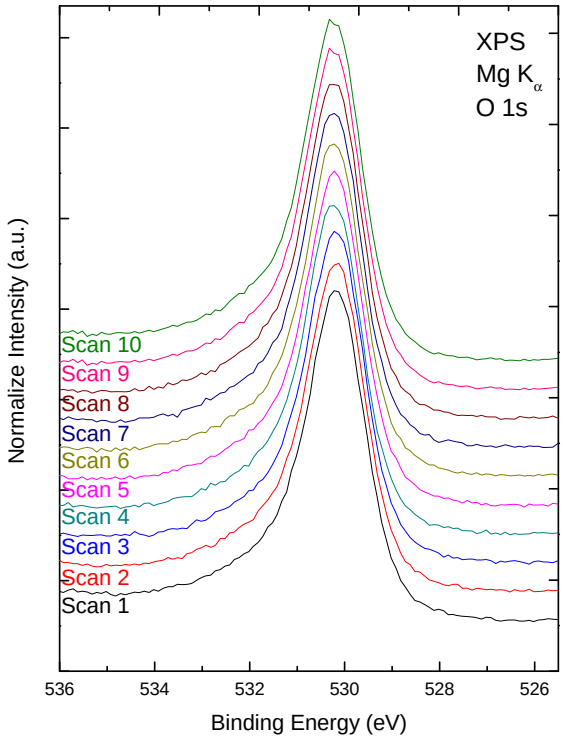

Figure 5.2: Series of O 1s XPS spectra to monitor possible beam-induced damage during a 4-hour radiation exposure.

Figure 5.2 above shows the spectra for ten scans of the O 1s peak taken over four hours of exposure to Mg K_α radiation at 1253.6 eV. The spectra are offset in a waterfall pattern for visual purposes only and show no appreciable deterioration in the O 1s signal over this time period. The Fe 2p peaks (Figure 5.3 below) show similar stability over the four hour exposure.

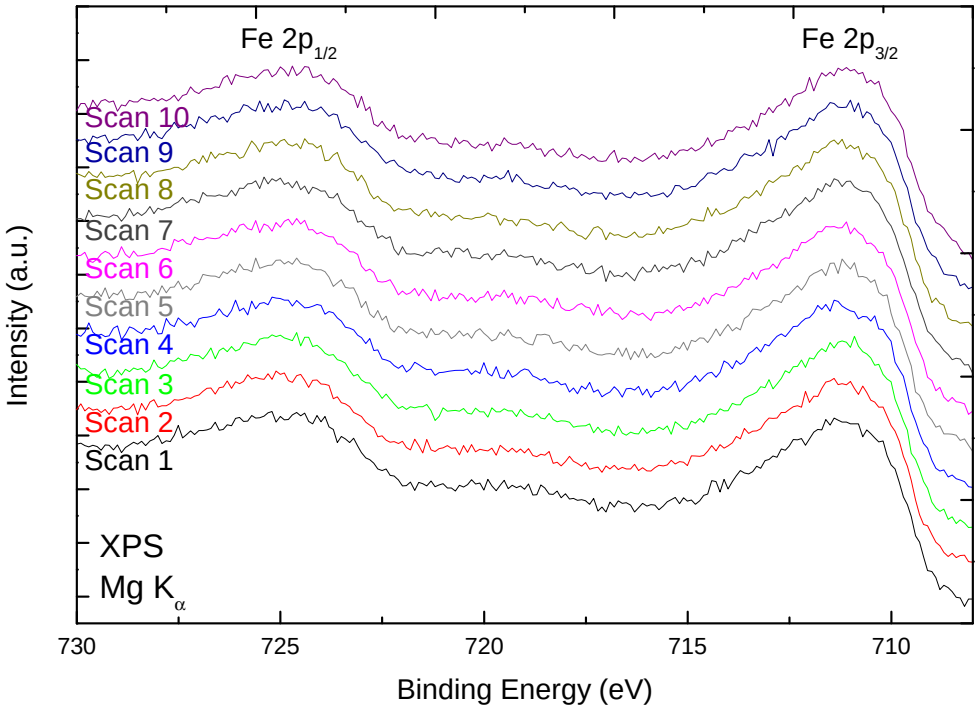

Figure 5.3: Series of Fe $2p_{1/2}$ and Fe $2p_{3/2}$ XPS spectra to monitor possible beam-induced damage during a 4-hour radiation exposure.

With no changes in shape or relative intensity in either the O 1s or Fe 2p peaks, the samples are proven to be durable enough for XPS experimentation and results can be presented as representative of the samples as provided.

This experimental series also confirms that the sample grounding technique described in Chapter 4 sufficiently allows charge transfer across the Fe_2O_3 surface, with no peak shifting due to charge buildup being shown in either of these spectra.

The α-Fe_2O_3 samples analyzed in this thesis were prepared by the McFarland Group at the University of California, Santa Barbara in three distinct batches, on three separate occasions. The October 2008 batch produced high performing PEC samples that have not since been reproduced, and is referred throughout this document as the "Mystery Sample". The first batch prepared specifically for UNLV's analysis was prepared in December 2008, and is referred to by sample numbers as described in Table 5.1 below.

Sample Name	Date Prepared	Fe thickness (as deposited)	Furnace name
"Mystery Sample"	October 2008	10 nm	Furnace 1
Sample 1	December 2008	10 nm	Furnace 1
Sample 2	December 2008	200 nm	Furnace 1
Sample 3	December 2008	400 nm	Furnace 1
Sample 4	December 2008	800 nm	Furnace 2
Sample 5	December 2008	0 nm	Not Calcined
Sample 6	December 2008	10 nm	Not Calcined
0 nm Control	May 2009	0 nm	Furnace 2
10 nm Control	May 2009	10 nm	Furnace 2
475 nm Control	May 2009	475 nm	Furnace 2

Table 5.1: Table of sample descriptions

Initial evaluation of the December 2008 samples showed prominent C 1s peaks, suggesting surface contamination. Because of the surface-sensitive nature of XPS

analysis, the formation of an overlayer due to contamination, improper handling, or air exposure may greatly impact the results obtained from XPS spectra. The May 2009 samples were thus prepared as control samples under nitrogen environment as described in Chapter 4, and the results of the clean packing procedure shown in Figure 5.4.

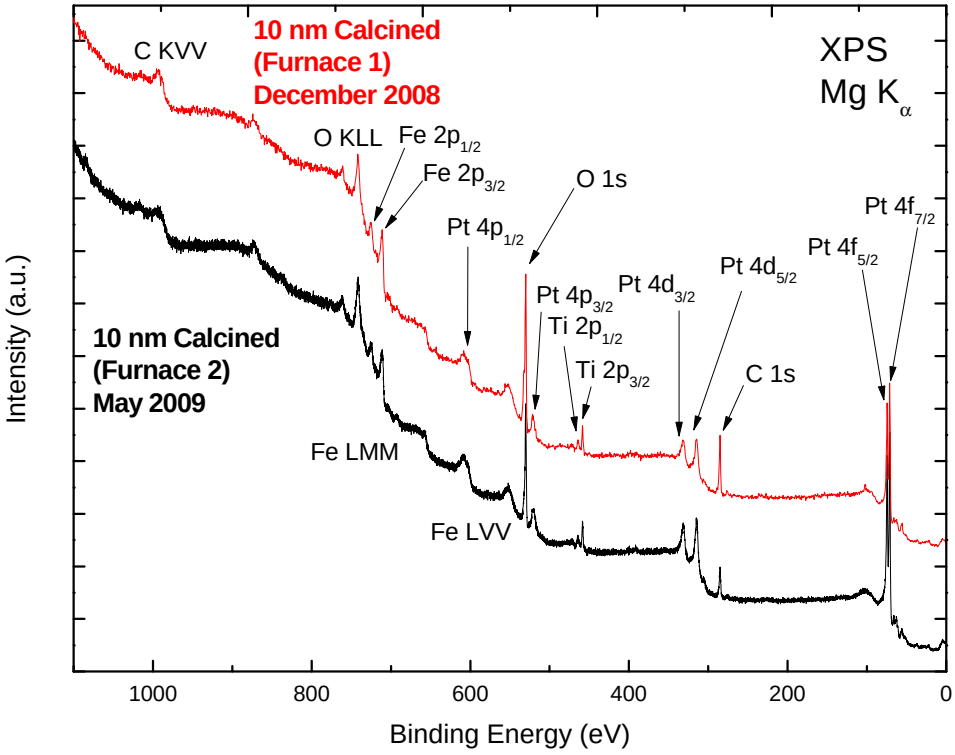

Figure 5.4: Impact of clean packing procedure on sample surface.

The two spectra in Fig. 5.4. were normalized to their background intensity at 200eV to discount differences in sample and x-ray source positions between measurements, and have been vertically offset to better show spectral details. The

10 nm sample surface prepared under the nitrogen environment (black spectrum) shows significantly less pronounced C 1s and O 1s peaks than the sample prepared in air (red spectrum), confirming that the packing procedure results in a cleaner sample. The cleaner sample also shows more prominent Pt 4f peaks, and further indicates decreased Pt signal attenuation due to the surface adsorbates.

It is important to note that the May 2009 control sample is not completely carbon-free; due to the fact that it was handled within the N_2 glovebag, i.e., without air exposure, we hypothesize that the carbon contamination possibly occurred during the growth process and not exclusively during the subsequent sample handling.

5.2 Sample Spectra Overview

The UCSB Fe_2O_3 samples were prepared on a quartz wafer, upon which were deposited 50 nm of Ti, 150 nm of Pt, and varying thicknesses of Fe. Figure 5.5 shows a model of the sample as grown.

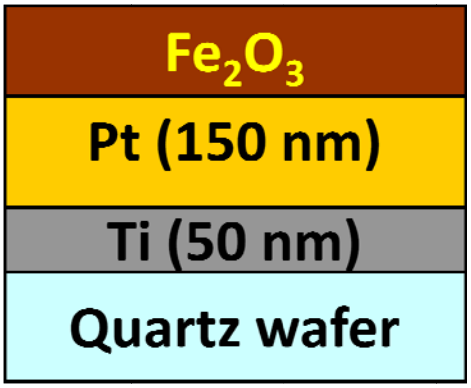

Figure 5.5: Model of UCSB Fe_2O_3 PEC sample.

Figure 5.6 shows an XPS spectrum of Sample 2, chosen as a representative Fe_2O_3 sample because its film thickness is the average of the thickest and thinnest samples analyzed. Note that the film thickness given here (200 nm) refers to the Fe film thickness before calcination (i.e., as deposited). It is the experience of the UCSB group that the resulting Fe_2O_3 film after calcination is approximately twice as thick.

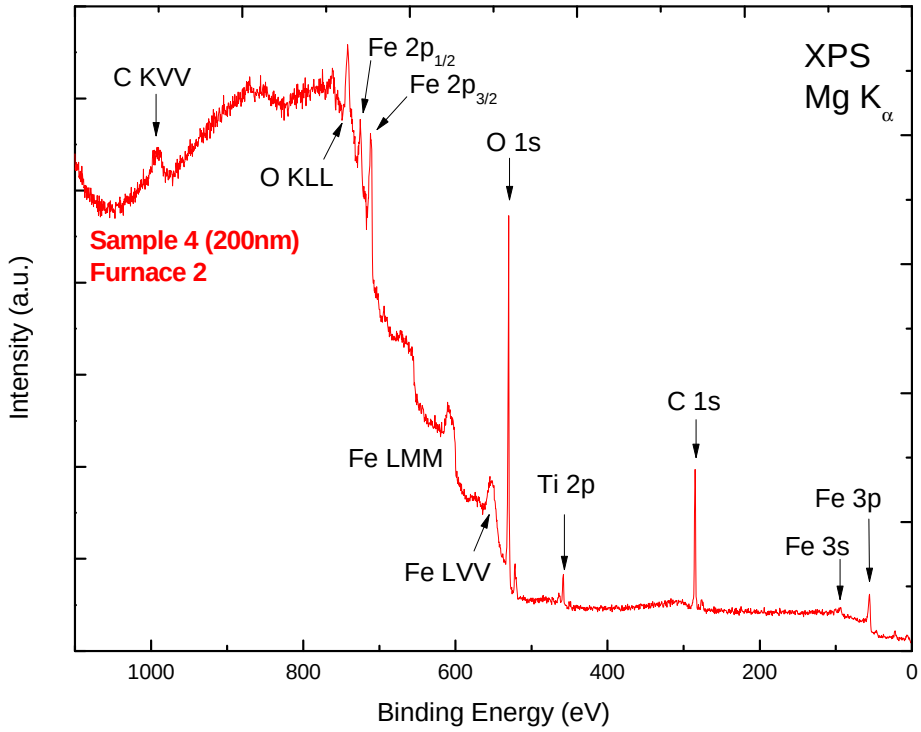

Figure 5.6: UCSB Sample 4, representative Fe_2O_3 PEC sample.

As would be expected for this sample, the Fe and O peaks dominate the spectrum, together with a substantial C 1s peak. The O 1s peak is pronounced and well defined, and peaks from several Fe orbitals are evident. The Ti peak, probably

due to Ti originating from the substrate, indicates the presence of diffusion processes, as will be discussed in more detail in an upcoming section. The high background on the high binding energy side of the spectrum is due to inelastic scattering of electrons stemming from deeper layers within the α-Fe_2O_3 sample (in essence, each characteristic emission line associated with atoms in the bulk of the sample creates a step function towards higher binding energy). A comparison of a 200 nm Fe sample with a 400 nm Fe sample is shown below in Figure 5.7 and Figure 5.8.

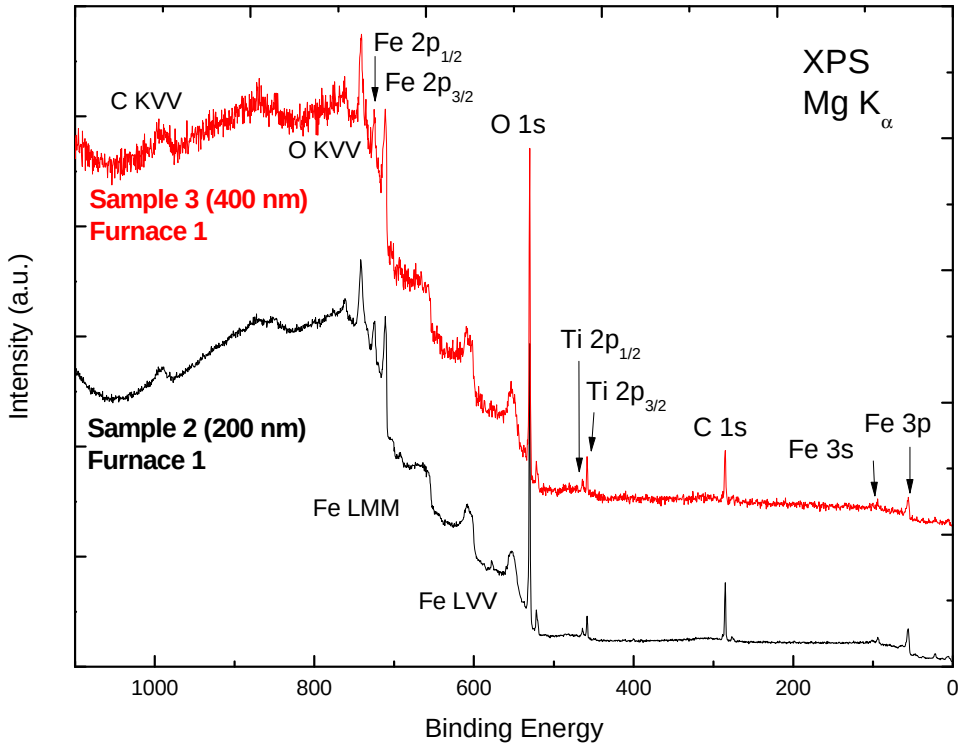

Figure 5.7: Comparison between Fe_2O_3 samples with 200 nm and 400 nm Fe film thickness before calcination.

The difference spectrum in Figure 5.8 was created by subtracting the spectrum of the thinner sample from that of the thicker sample, more clearly highlighting the differences between these samples. Due to the normalization to the background at 200 eV, the difference spectrum is close to zero in this range. The difference spectrum also reveals the comparatively higher oxygen content of Sample 3 versus Sample 2, and a slightly increased amount of Ti on the surface.

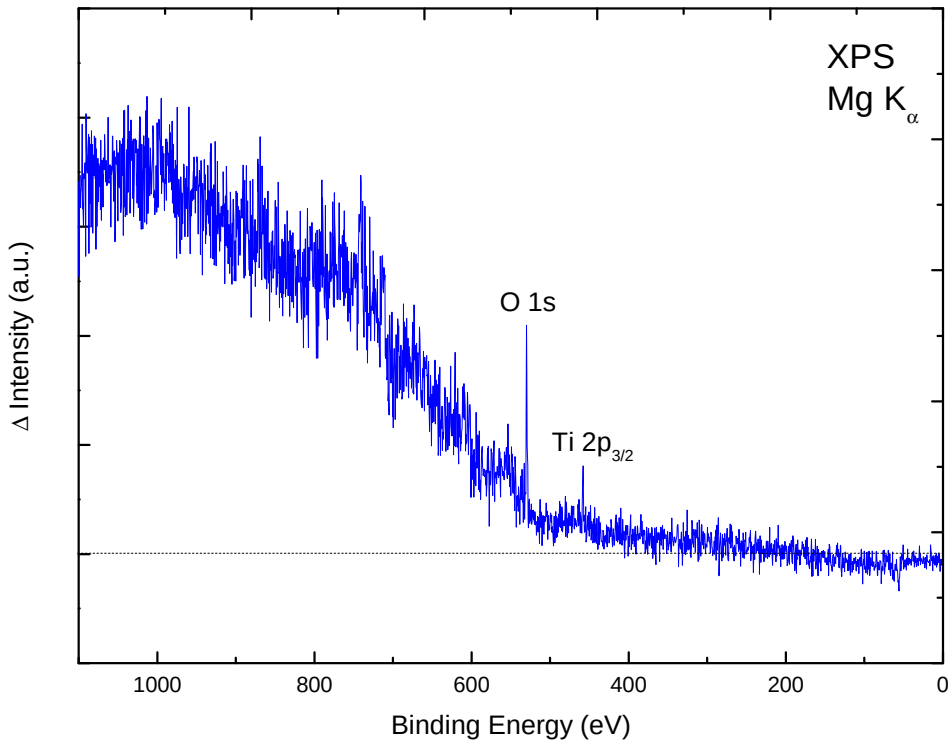

Figure 5.8: Difference spectrum of Sample 2 versus Sample 3.

The full series of the December 2008 survey spectra is plotted in Figure 5.9. Survey spectra present an overview of the entire energy range and are useful for quickly

estimating the composition of samples. The spectra shown have been normalized to the background at 274 eV, and offset vertically to facilitate comparison. Calcined samples (1-4) are indicated by bold font.

Beyond the expected iron, oxygen, and carbon, the survey spectra also reveal the presence of chromium (for Sample 2 and Sample 3) and titanium (for all calcined samples). Although Mg K_α XPS has an information depth of only a few nanometers, and Ti should be buried under a minimum of 150 nm of Pt and varying thicknesses of Fe (or Fe_2O_3), the spectra of this surface-sensitive technique clearly show the presence of titanium on the surface of the calcined samples. Tellingly, titanium does not appear to be present on the surfaces of the non-calcined samples. This indicates significant diffusion processes during the calcination process, as will be described below. Note that the thinnest sample (sample 1, 10 nm nominal Fe thickness) also exhibits peaks characteristic of platinum, which suggests that the formed Fe_2O_3 overlayer is not a completely homogeneous, 20-nm-thick layer, but (at least in some regions) allows XPS to detect Pt atoms either through the Fe_2O_3 or in regions between Fe_2O_3 islands. A diffusion of Pt atoms to the surface can also not be ruled out, but is less likely, since it is not seen for any of the other (thicker) samples.

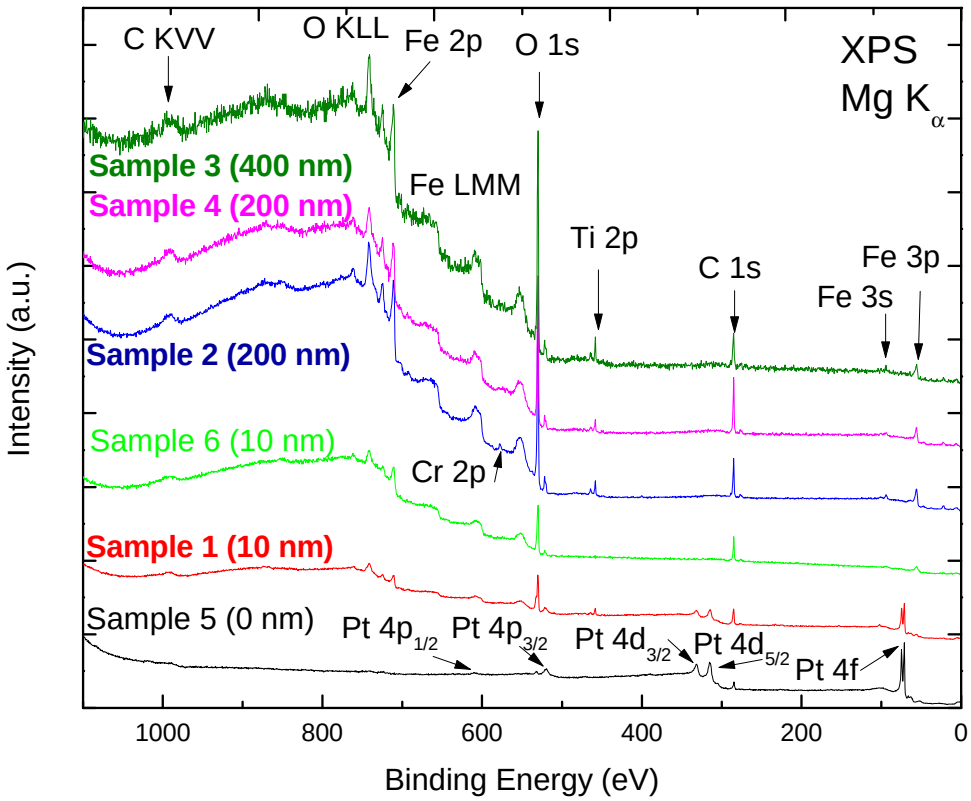

Figure 5.9: Survey spectra of December 2008 samples.

Since Ti appears only in samples that have been calcined (heated), additional experiments investigating the effect of temperature on the samples were performed and are described in Section 5.3.

5.3 Sample Preparation Findings

5.3.1 Effect of Calcination on Morphology

October 2008 and December 2008 samples were annealed at 700°C for 4 hours with a 2°C ramp up in temperature to operating temperature. After 4 hours, the furnace was automatically turned off with no controlled temperature ramp down.

For the May 2009 samples, the furnace failed to turn off after 4 hours and this batch was calcined for 8 hours.

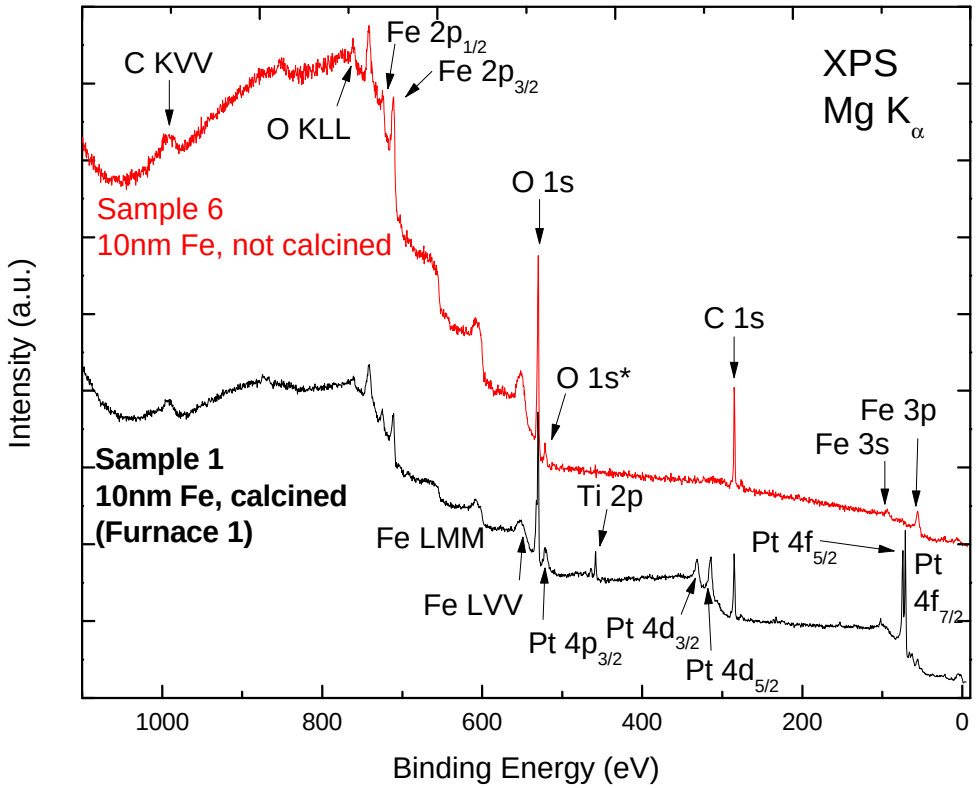

Figure 5.10: Comparison of 10 nm films, calcined (bottom) and not calcined (top).

As seen with all calcined samples, the XPS spectrum of the calcined 10 nm film shows Ti 2p peaks; in addition, strong Pt peaks are also present. In contrast, neither Ti nor Pt peaks are visible for the not-calcined sample. Apparently, a 10 nm-thick Fe overlayer is beyond the limit for Pt (and Ti) detection with Mg K_α XPS (keeping in mind that the effective information depth is a function of kinetic energy of the photoelectrons), such that the Pt atoms buried under 10 nm of Fe (and

consequentially approximately 20 nm of Fe_2O_3) should not be visible. Spectra for both these samples were taken at the same incident angle to the x-ray source, so angular effects can be ruled out. Furthermore, since the Pt layer is not visible in the uncalcined samples, porosity of the as-deposited film can also be ruled out; however, a morphology change in the film due to heating may be occurring.

To examine the morphological differences between otherwise identical calcined and uncalcined films, Atomic Force Microscope (AFM) images were taken of the two samples. Samples were removed from vacuum for imaging after completion of all XPS experiments. Figure 5.11 and Figure 5.12 show the surface morphology of the 10 nm uncalcined Sample 6.

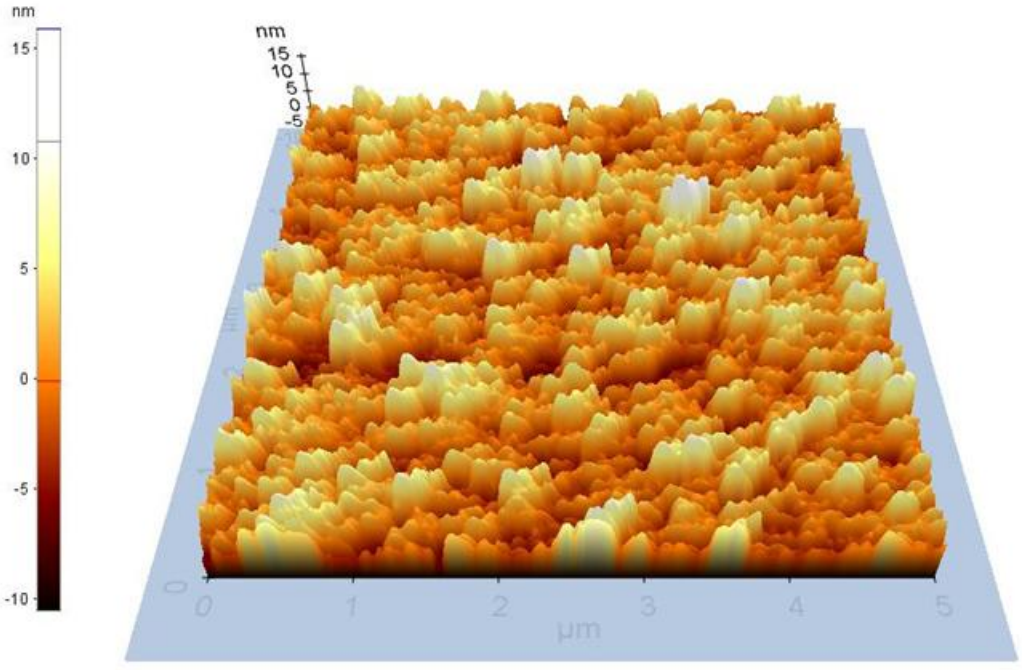

Figure 5.11: $(5\ \mu m)^2$ AFM image of the 10 nm thick uncalcined Fe film.

The image in Figure 5.11 is a (5 μm)^2 view of Sample 6, and was taken in Contact Mode with a scan rate of 0.5 Hz. Although there are small islands approximately 10 nm in height, the film is generally uniformly even (note the difference in scale for the x/y- and z-axes). A (50 μm)^2 view of the same region shows that this holds true even at the more macroscopic level, and is shown in Figure 5.12.

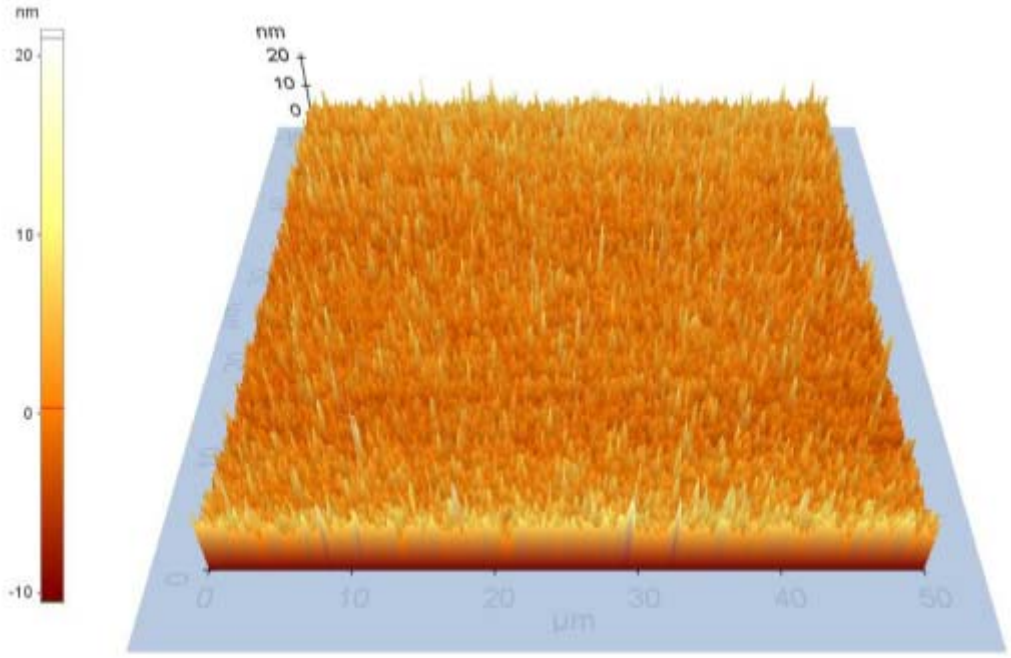

Figure 5.12: (50 μm)^2 AFM image of the 10 nm thick uncalcined Fe film.

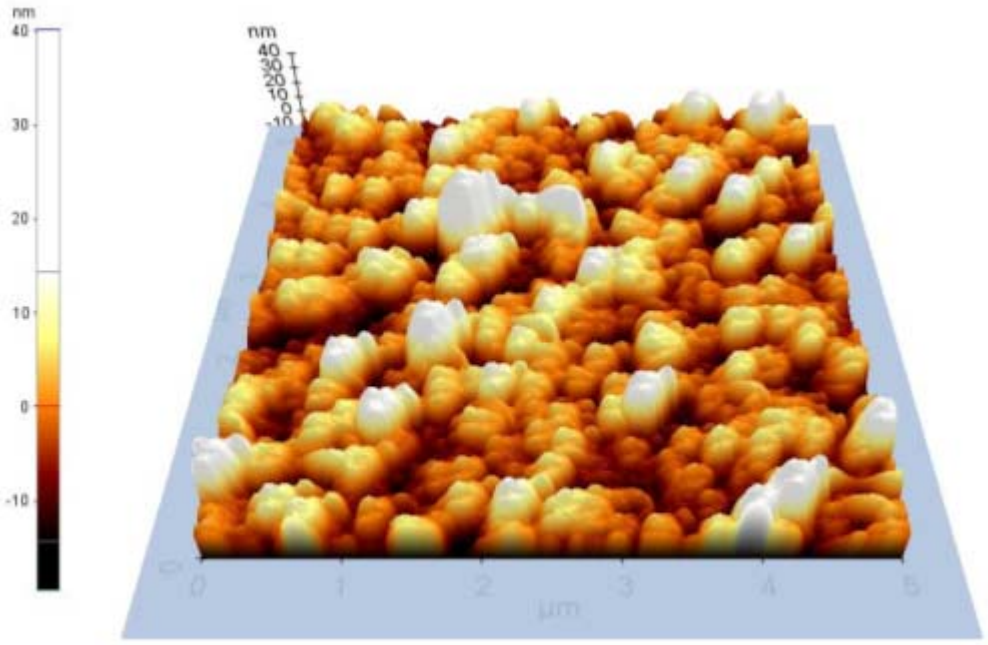

Figure 5.13: $(5\ \mu m)^2$ AFM image of the 10 nm thick calcined Fe_2O_3 film.

After calcination at 700 °C for 4 hours, distinct changes to the surface of the film are seen, as shown in Figure 5.13. shows increased island growth, with peaks approximately 30 nm in height (i.e., about three times as high as in the uncalcined case in Figure 5.11). The AFM image also shows more regions with negative depths. This may be due to several reasons – island formation is occurring at the Fe_2O_3 layer and there is a dewetting effect that reveals the substrate as the island grows. This would explain the Pt peaks in the XPS spectrum of the calcined 10 nm film, but does not account for the presence of Ti. Alternatively, this island formation and its corresponding holes may be due to the outgrowth of either the Pt or Ti layers into and through the Fe_2O_3 layer.

To better investigate these theories, it is necessary to better understand the Ti/Pt interface without the additional Fe/Fe_2O_3 variables. This was done by heating 0 nm Fe (i.e., bare Pt film) samples to different temperatures and by studying the surface composition in XPS survey scans. These spectra were also compared against a reference Pt foil, as shown in Figure 5.14.

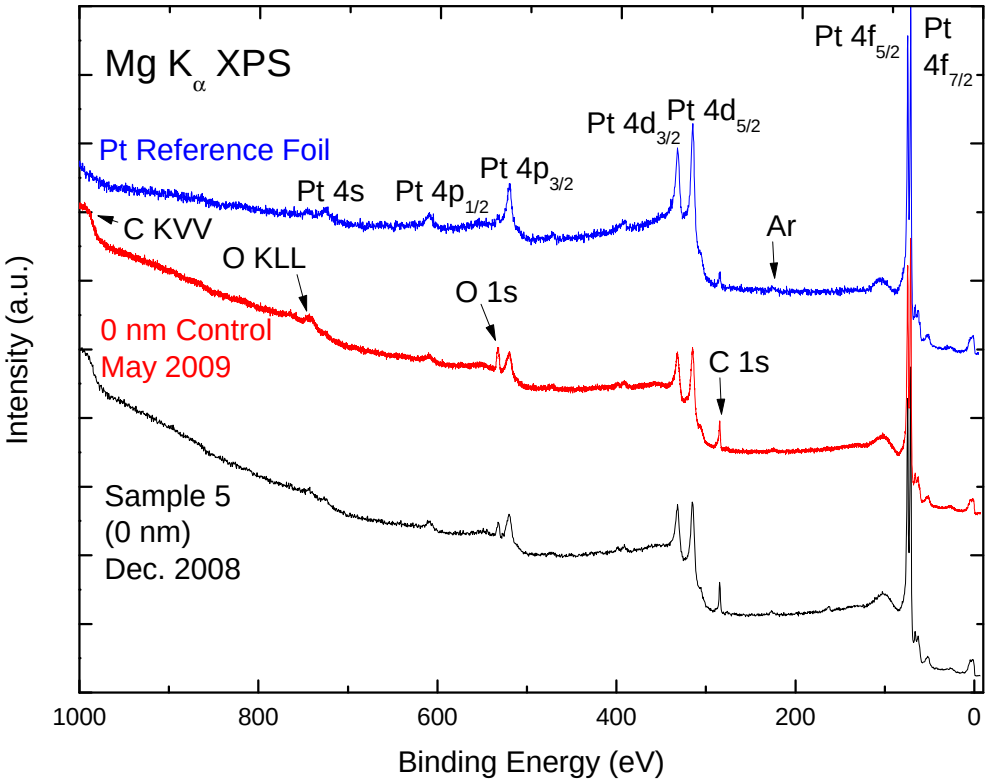

Figure 5.14: Comparison of reference Pt foil to Pt film samples.

The reference Pt foil was sputtered with Ar^+ ions at 3 keV for 3 hours to clean its surface before XPS examination. This results in a small Ar peak present in the reference spectrum that is not seen in the other two samples. The O 1s and C 1s

peaks seen in the grown samples are more prominent than in the sputter-cleaned reference foil, but similar to each other, regardless of the sample handling and extraction method. In fact, the O 1s signal of the 0 nm control sample is somewhat larger, despite the fact that it was extracted under dry nitrogen conditions.

One of the May 2009 0 nm control samples was heated in air at 700°C in a Lindberg/Blue M furnace for 4 hours and examined by XPS in the VG SCIENTA system (to be discussed in conjunction with Figure 5.22). Another May 2009 0 nm control sample was directly heated in vacuum in 100°C increments for 30 minutes, and immediately measured by XPS using the monochromatized Al K_α x-ray source. The corresponding data is shown in Figure 5.15.

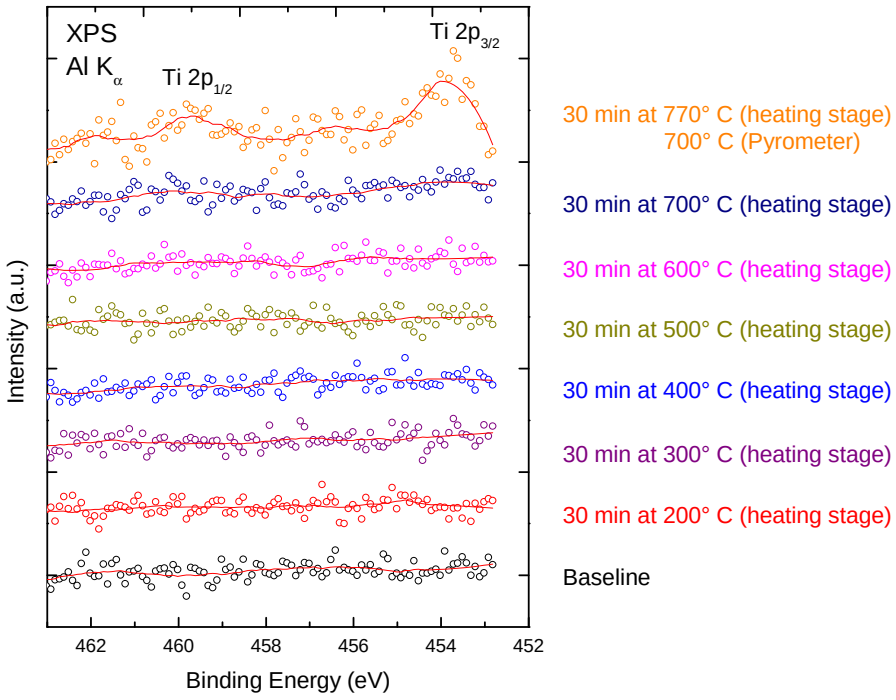

Figure 5.15: Emergence of Ti 2p peak in response to heating of a May 2009 0 nm control sample in UHV.

The sample temperatures given were measured by the thermocouple of the heating stage (indicated by "heating stage" in Figure 5.15). For the highest temperature, the sample temperature was also measured directly with a pyrometer. Comparison of the displayed thermocouple-measured temperature versus the pyrometer-measured temperature showed readings of 770°C and 700°C respectively. Since the samples are heated from below, the poor thermal conductivity of the quartz substrate may account for this difference.

As is evident from Figure 5.15, Ti 2p peaks emerge after heating the sample to 700 °C on the pyrometer/sample surface scale (770°C on the thermocouple scale), while they are absent after annealing at 700 °C on the thermocouple scale. Apparently, Ti diffusion is initiated between 600°C and 700°C on the pyrometer/sample surface scale.

In addition to the temperature dependence, it is important to understand the time dependence of the observed Ti diffusion. To gain insight, an additional sample was heated at 705 °C (on the pyrometer/sample surface scale) for 4 hours and compared to a sample that was heated for 30 minutes at 700 °C (again on the pyrometer/sample surface scale). The results are shown in Figure 5.16. Apparently, a pronounced Ti signal is present already after 30 minutes of annealing, indicating that the process is relatively fast.

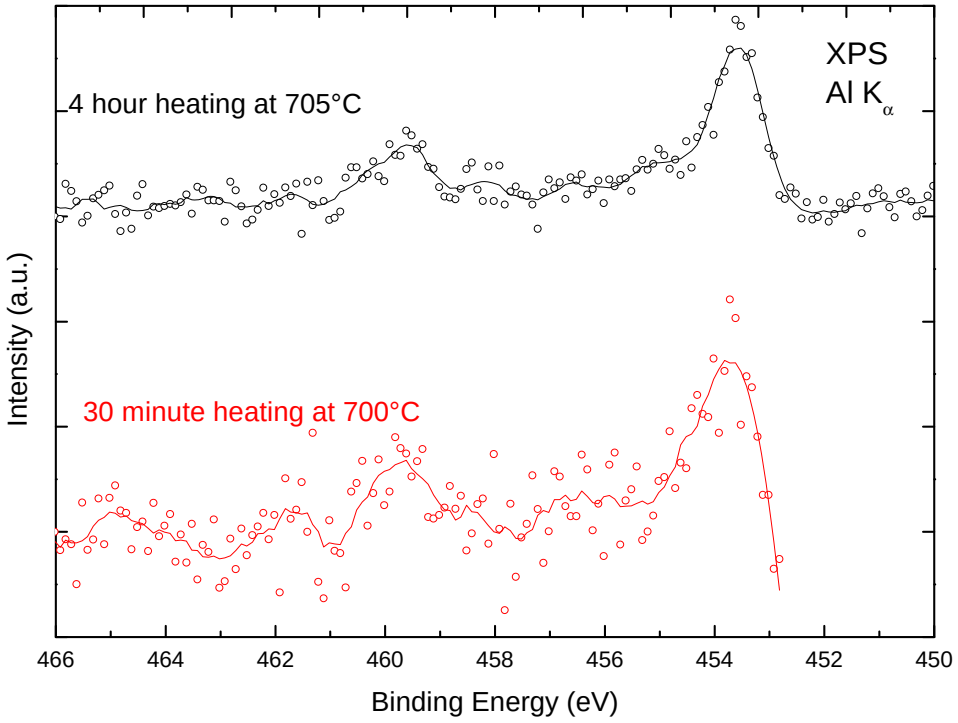

Figure 5.16: Ti 2p XPS spectra after heat treatment, showing the emergence of a Ti signal from atoms diffusing to the Pt surface already during 30 minutes of heating at 700 °C.

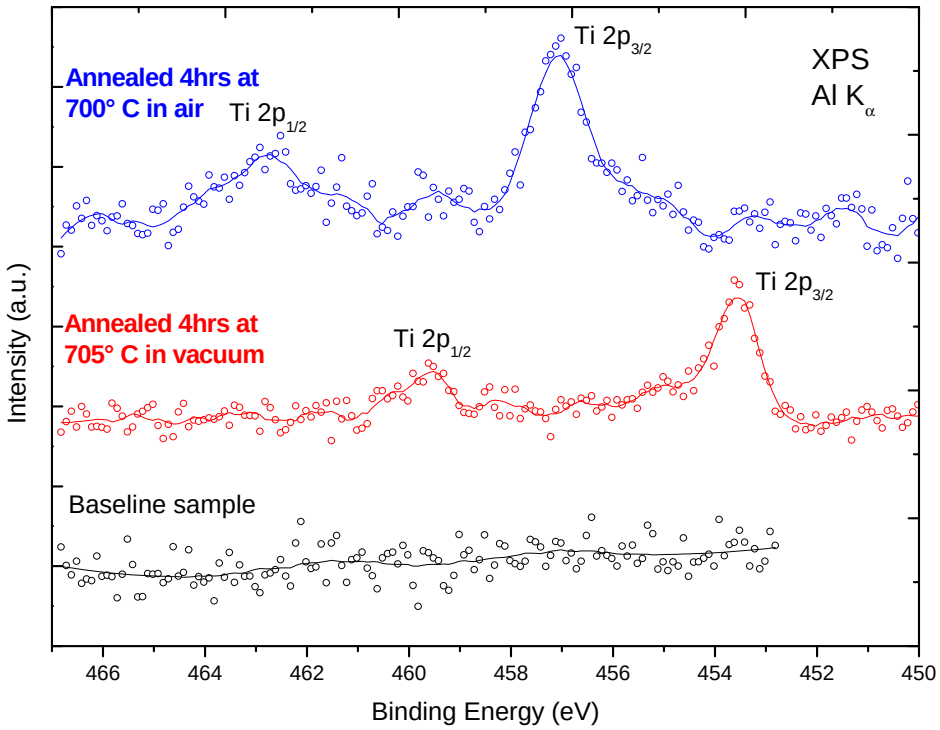

Figure 5.17: Ti 2p spectra of a 0 nm Fe control sample before annealing (bottom), after annealing in UHV (center, 705 °C, pyrometer temperature scale) , and after annealing in air (top, 700 °C).

Finally, comparing a sample heated in air for 4 hours versus one heated in vacuum for 4 hours completes the picture, as shown in Figure 5.17. Comparing the unannealed baseline sample (bottom), with the two spectra obtained after annealing in UHV (center) and air (top), it is evident that the Ti peaks emerge as a response to the annealing step. The sample annealed in vacuum shows the Ti $2p_{3/2}$ peak at 453.6 eV (b.e.), indicating metallic titanium, whereas the sample annealed in air has a Ti $2p_{3/2}$ peak position of 457.0 eV – indicative of a titanium oxide, most likely an intermediate form of TiO_2.

Scanning Electron Microscope (SEM) images were taken at UCSB to shed further light on the morphology of the PEC samples as a function of heating.

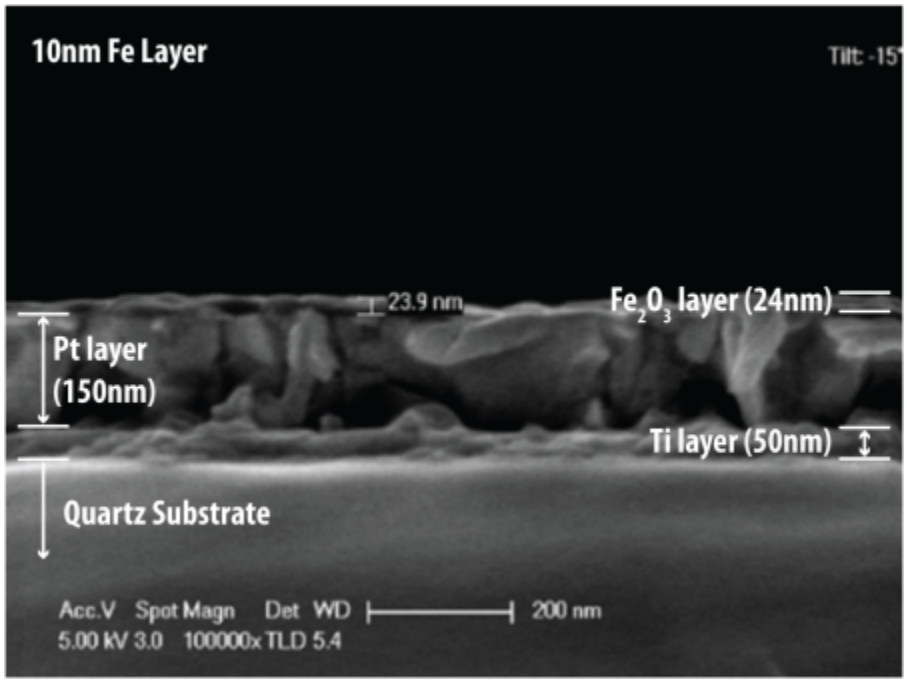

Figure 5.18: UCSB SEM image of the 10 nm Fe calcined PEC film (cross section).

Figure 5.18 shows a cross sectional view of a 10 nm Fe sample after calcination. Consistent with previous PEC Fe_2O_3 samples, the Fe layer has roughly doubled in thickness and, in this sample, is 23.9 nm thick. This thin sample shows an apparent delamination between the Pt layer and the Fe_2O_3 layer, and some grain structure formation is evident within the Pt layer

An SEM top-down view of the sample in Figure 5.19 shows a porous, small grained structure with some island formation (as seen in Figure 5.13), but accretion is not yet pronounced.

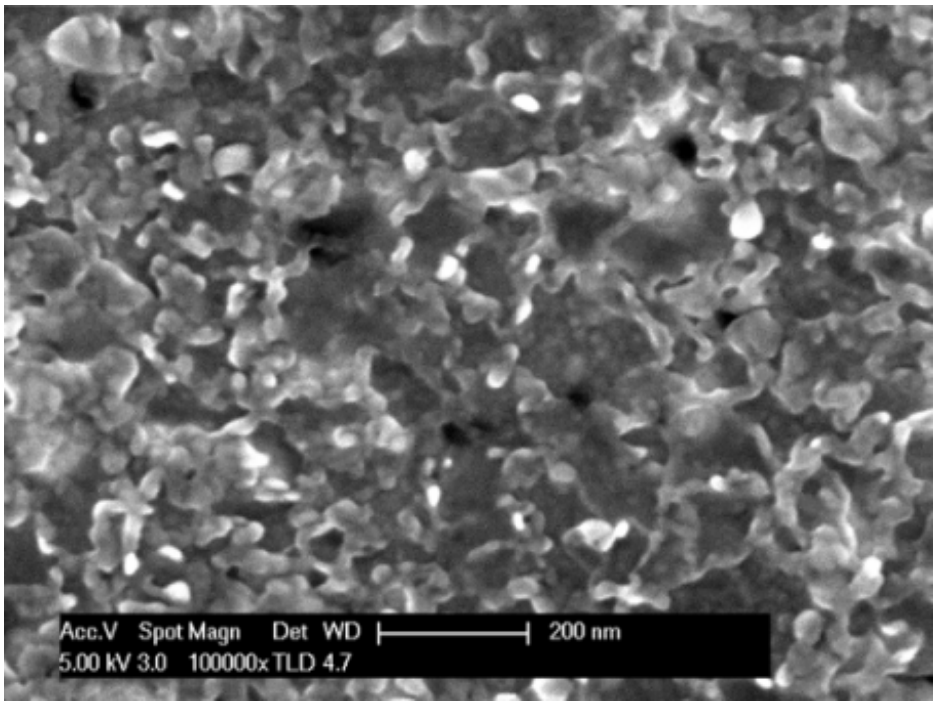

Figure 5.19: UCSB SEM image of 10 nm Fe calcined PEC film (top view).

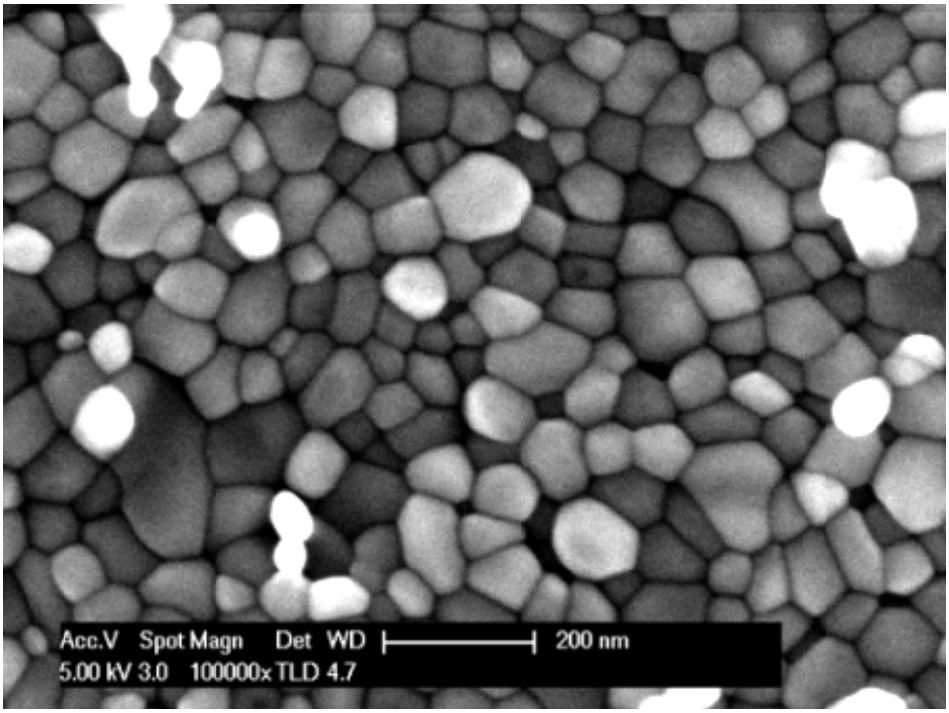

Figure 5.20: UCSB SEM image of 200 nm Fe PEC film (top view).

The surface of the 200 nm film is more uniformly covered by pebble-like Fe_2O_3 particles than in the 10 nm film, but, as shown in Figure 5.7, Ti signals are still present in its XPS spectrum. A cross-sectional SEM image of this sample (Figure 5.21) shows that the iron oxide film is porous in its bulk, and large cavities exist immediately at its interface to the Pt layer.

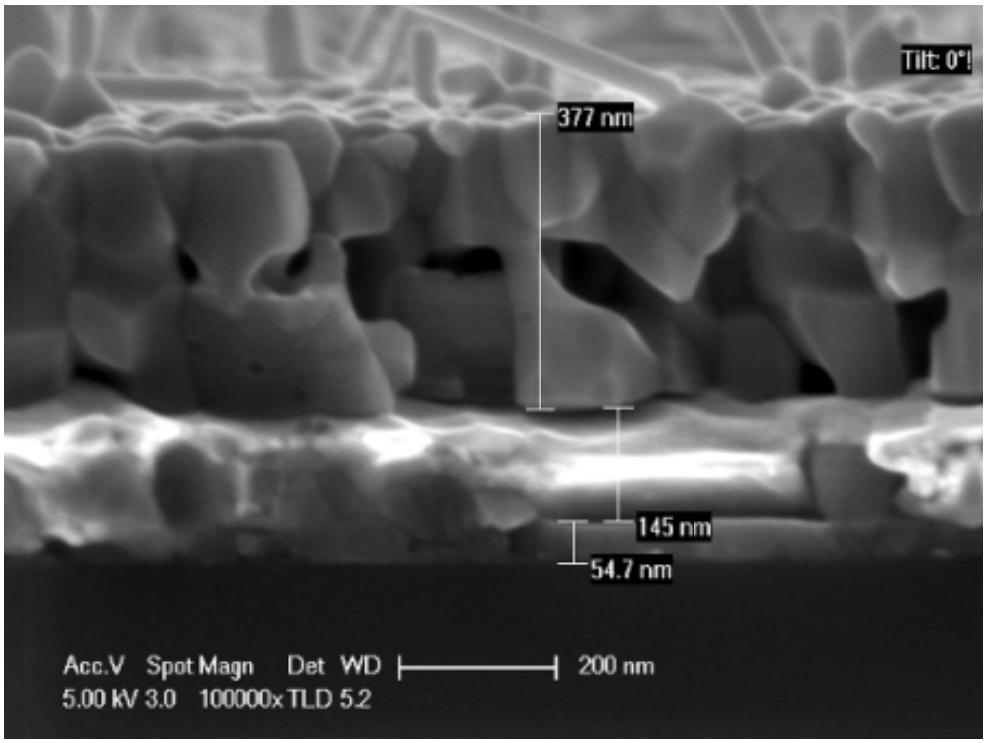

Figure 5.21: UCSB SEM image of 200 nm Fe PEC film (cross section).

The interface between the Ti and Pt layers is less distinct than in the 10 nm sample. Large needle-like outcroppings with diameters less than 20 nm are visible on the surface of the 200 nm film, and AFM analysis (Figure 5.22) shows that the observed islands reach up to 80 nm in height.

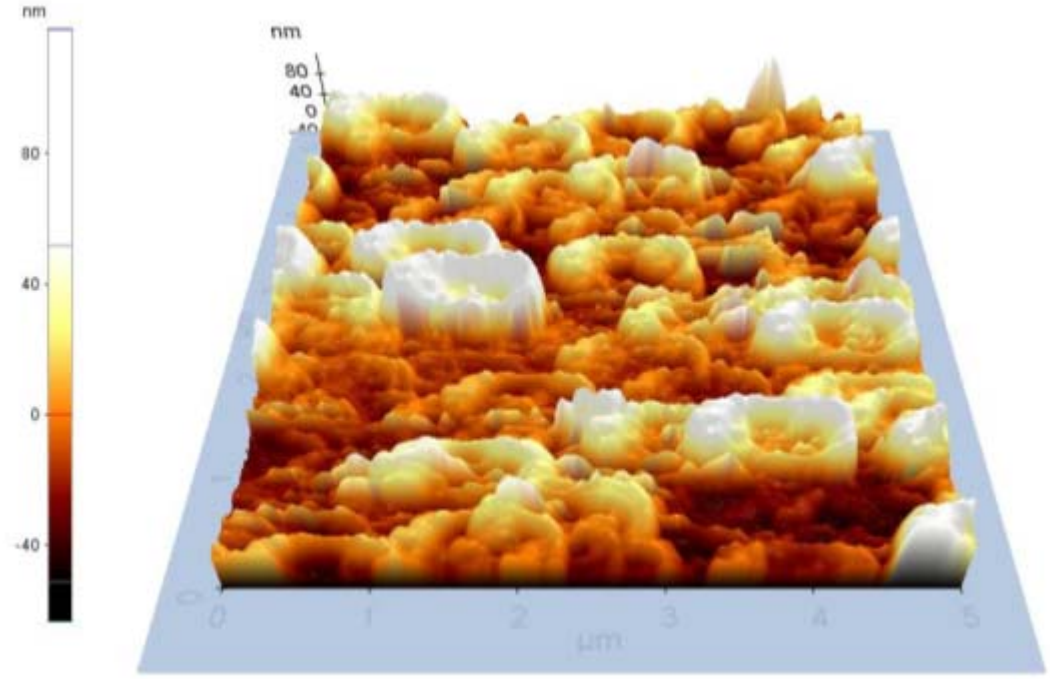

Figure 5.22: AFM image of 200 nm Fe PEC film

5.3.2 Activity of Fe Due to Calcination

During the May 2009 sample preparation, "0 nm" samples (i.e., Pt films without Fe coverage) were calcined in Furnace 1 within the same tube as the 10 nm and 475 nm samples. The XPS spectrum for this 0 nm sample is presented in Figure 5.23. The complete lack of Pt peaks and presence Fe in the spectrum is puzzling, for even the thinnest calcined Fe films exhibit a noticeable Pt signal in XPS (Figure 5.24). In fact, this nominally iron-free sample shows better Fe film coverage than the 10 nm sample. A comparison between the uncalcined and calcined XPS spectra (Figure 5.25) shows significant changes occurring during this specific calcination.

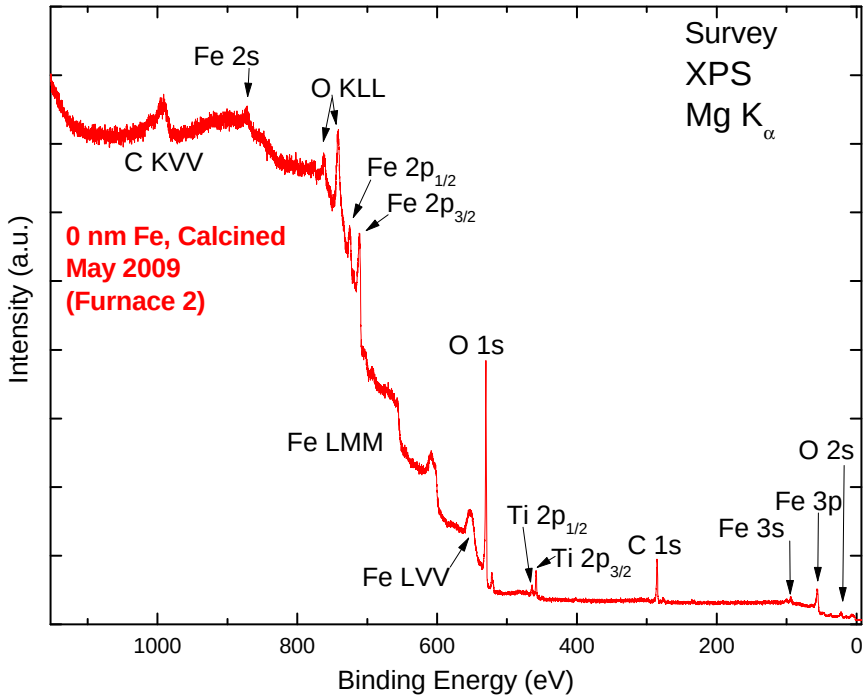

Figure 5.23: XPS spectrum of May 2009 0 nm calcined sample.

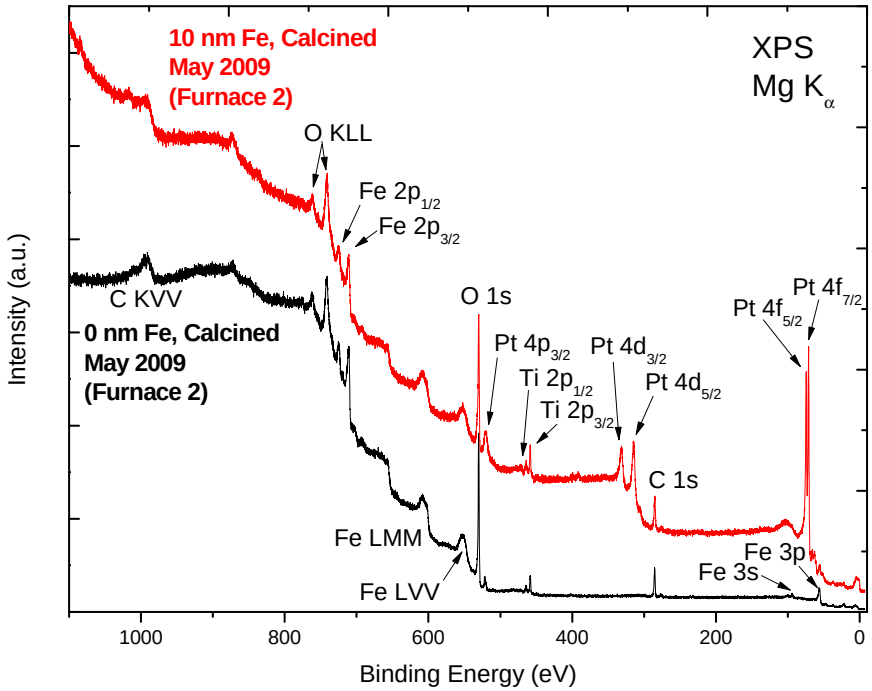

Figure 5.24: Comparison between 0 nm and 10 nm calcined samples.

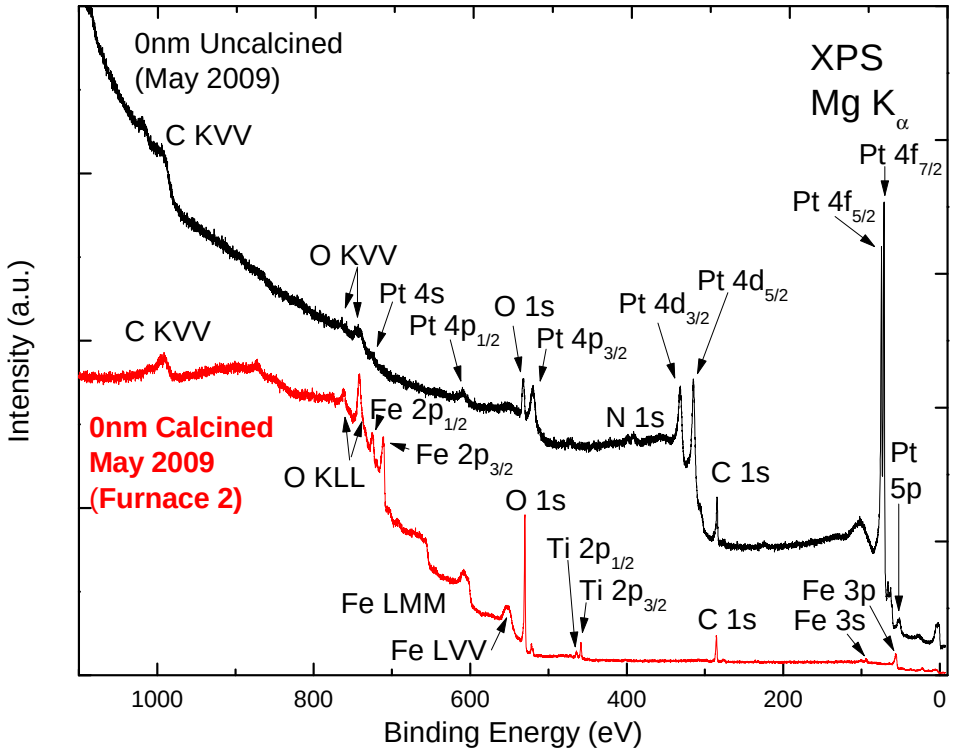

Figure 5.25: Comparison between uncalcined and calcined 0 nm samples.

To rule out experimental error and possible sample mix-up, the 0 nm sample was compared against a photograph of the samples being prepared in the Furnace 1 (Figure 5.26). The 0 nm sample measured by XPS is indicated with a red arrow and starred (*) in the image below. The distinctly curved shape of the 0 nm sample was further verified by comparing the photograph to lab notes taken during preparation.

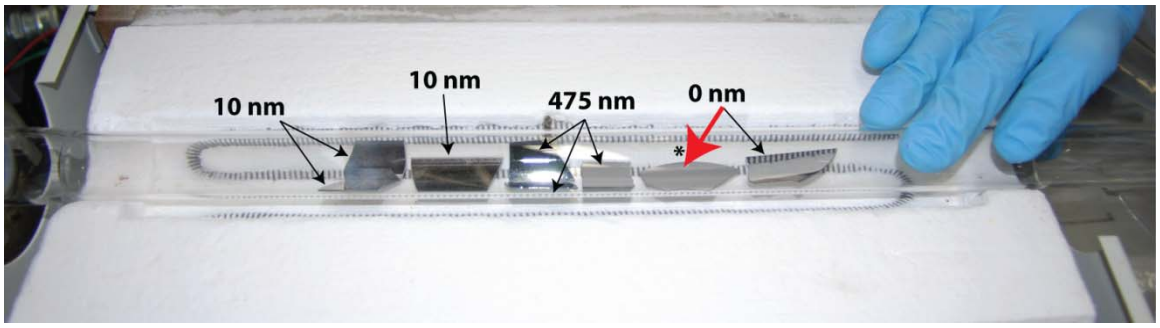

Figure 5.26: Sample positions during calcination

The position of the 0 nm sample immediately adjacent to the 475 nm sample suggests that, during the calcination process may have desorbed from the 475 nm samples and readsorbed (calcined) on the 0 nm sample, explaining its complete coverage with iron oxide. This finding may also suggest a pathway through which other contaminants may have been introduced into the Fe_2O_3 samples.

5.3.3 Sample Contamination

Secondary Ion Mass Spectrometry (SIMS) analysis performed at UCSB revealed several contaminants in the calcined films. A December 2008 SIMS analysis reported the presence of Cr and Al. These contaminants were seen in films of different thicknesses, both before and after calcination – however, the relative abundance of these contaminants appeared to be higher after the heating process.

The McFarland group suspected the contamination came from the Pt layer, and UNLV was asked to confirm their findings with our experimental techniques. Although the SIMS technique is extremely sensitive with detection limits on the order of parts per billion, it is a destructive technique that does not shed information about the surface of the sample, whereas XPS preserves the as-grown

state of the sample, but gives composition information with much lower sensitivity (approx. 0.1%).

The primary Al 2p XPS peak was not useful in these experiments because of its position at 74.4 eV, directly under the dominant Pt $4f_{7/2}$ and Pt $4f_{5/2}$ peaks at 71 and 74 eV, respectively. The Al 2s peak at 118 eV (b.e.), however, was in a binding energy region unobscured by other elements. Since the Pt layer was the suspected cause of contamination, this region of the platinum-surfaced Sample 5 was examined, as shown in Figure 5.28. No indication of an Al peak was found, and inspection of the other samples showed the same result, as shown in Fig. 5.29.

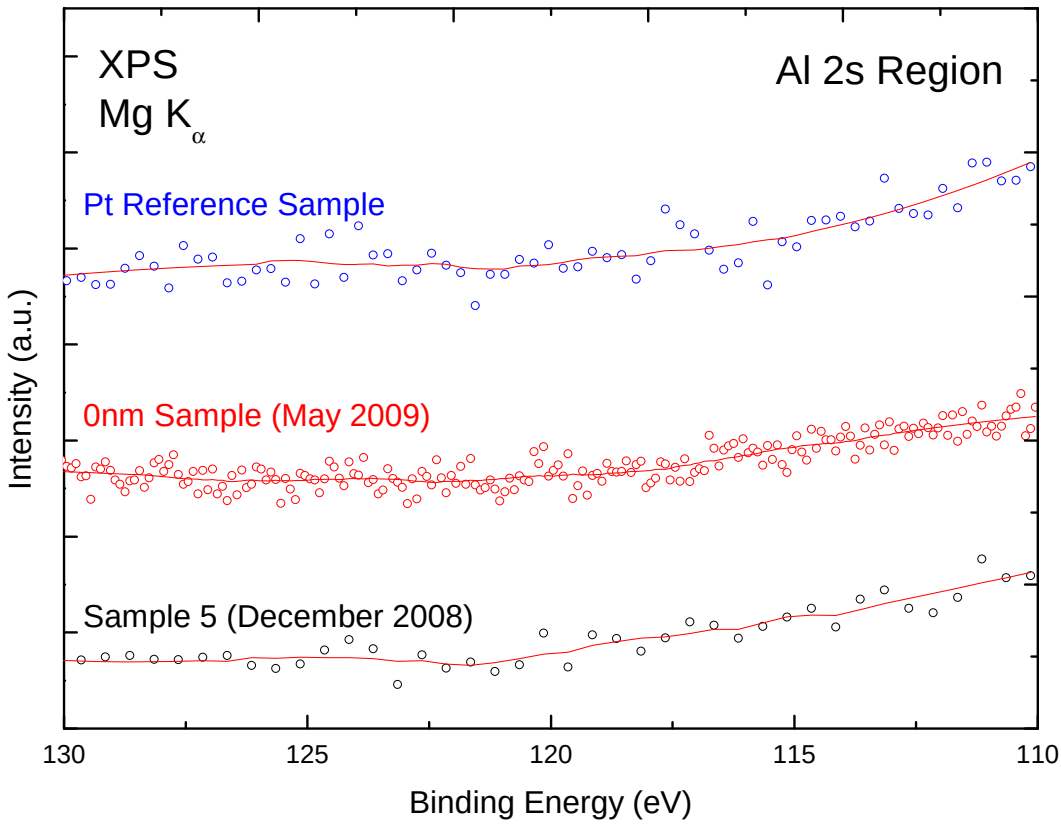

Figure 5.27: XPS spectra of the Al 2s region of Pt samples.

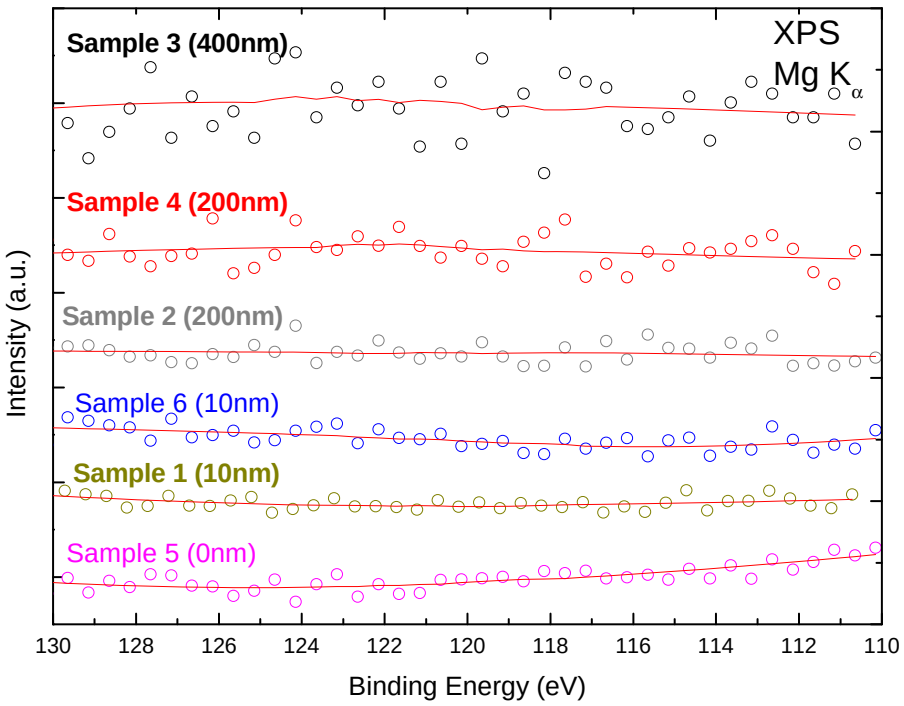

Figure 5.28: XPS spectra of the Al 2s region for December 2008 samples.

Initial survey spectra of the December 2008 samples (Figure 5.9) confirmed the presence of chromium on Samples 2 and 3, both calcinated in the Furnace 1. Detail spectra of the Cr 2p region (Figure 5.30) indeed show enhanced spectral intensity in this region for samples 2 and 3, but do not unambiguously show the presence of Cr in any other sample (within the noise level).

The diffusion method described in Section 5.3.2 may account for the presence of Cr in the Furnace 1 samples but not in the Furnace 2 samples. During sustained heating cycles, desorption of contaminants from walls and samples may contaminate and be transported through the furnace's heating tube and adsorb unto other samples. This cycle of desorption, transport, and adsorption may not only affect samples of any particular batch – it can affect other samples prepared after

contamination. It is therefore possible that Furnace 1 contains trace amounts of Cr from previous annealing steps.

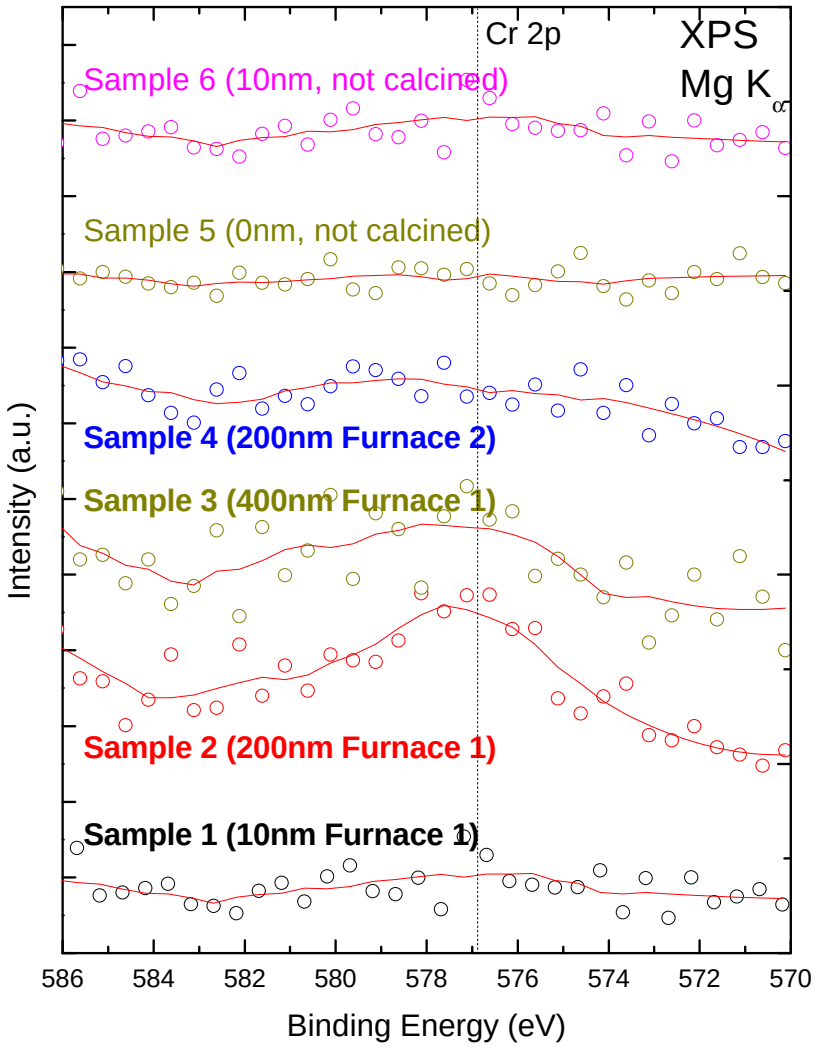

Figure 5.29: XPS spectra of the Cr 2p region for December 2008 samples. Open circles denote data points, while solid lines were obtained from a Savitzky-Golay smoothing procedure (2nd order polynomial, 13 data points).

5.4 Furnace 1 and Furnace 2 Sample Differences

With known performance differences between otherwise identical samples calcined in Furnace 1 and Furnace 2, it appears that the calcination process itself is introducing differences into these samples in the form of contamination. Figure 5.31 presents the spectra for two 200 nm samples calcined for 4 hours at 700°C in the respective furnaces.

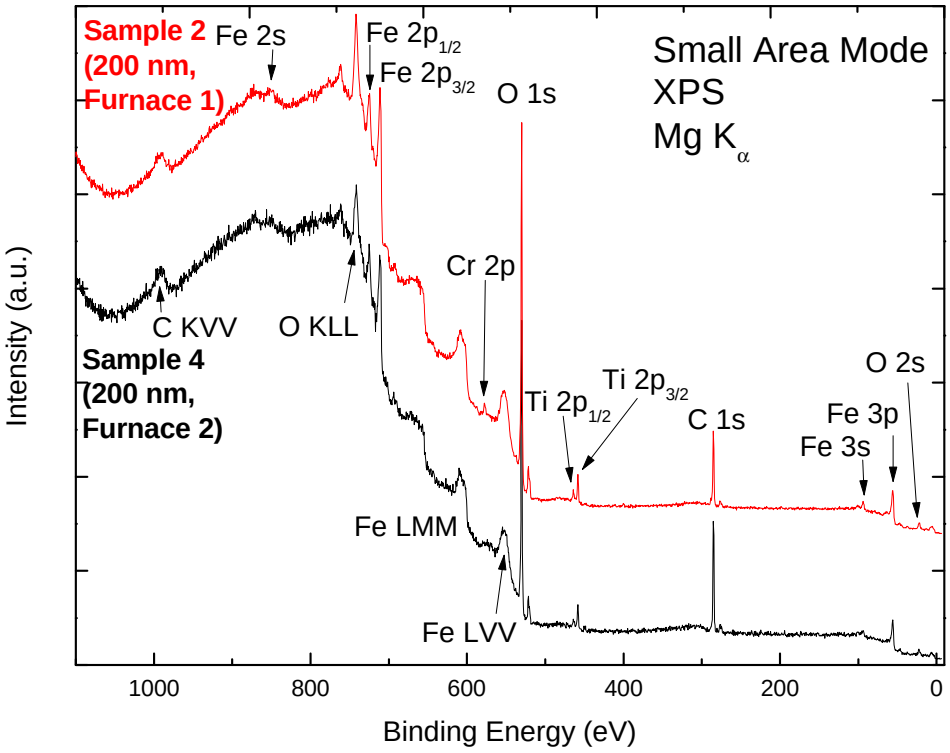

Figure 5.30: XPS spectra of Furnace 1 and Furnace 2 samples.

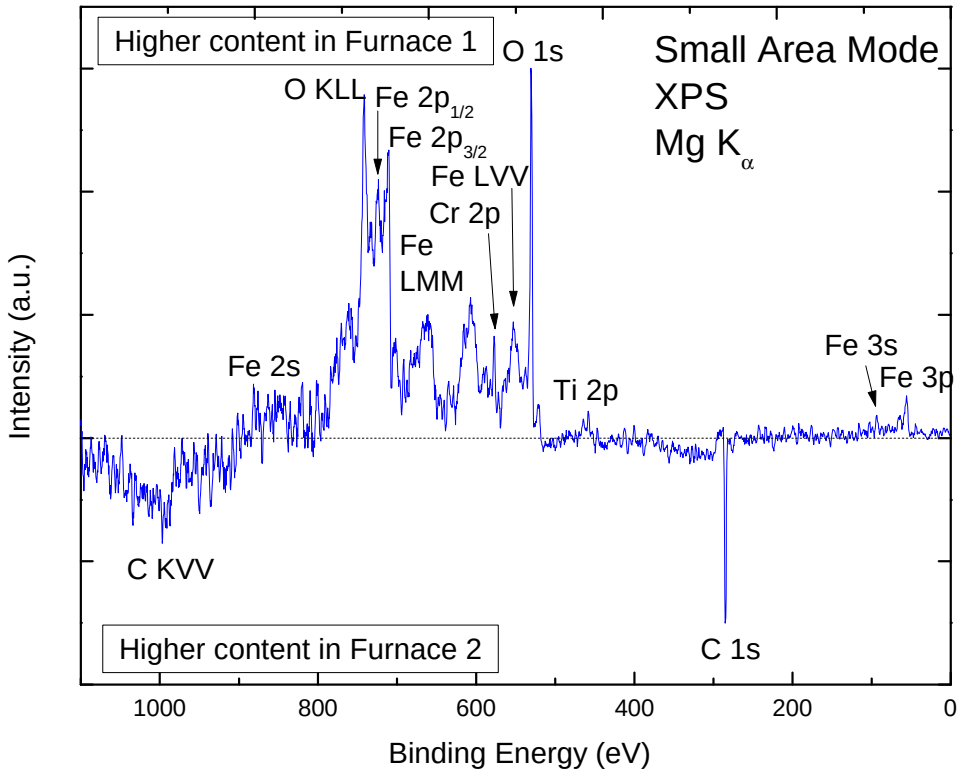

Figure 5.31: Difference spectrum of Furnace 1 and Furnace 2 samples.

Both samples show strong iron, oxygen, and carbon peaks. As with the other calcined samples, the Ti 2p peaks are present in these spectra, but no Pt is visible. The Furnace 1 sample also shows a distinct Cr 2p peak that is not present in the Furnace 2 sample.

The difference spectrum shown in Figure 5.32 was created by normalizing both spectra to the low binding energy background at 200 eV, and subtracting the Furnace 2 data from the Furnace 1 data. The dotted line was added as a visual reference to the baseline. The Furnace 1 sample shows higher iron and oxygen content than the Furnace 2 sample. The Furnace 2 sample, however, has a higher

carbon content. As will be discussed in Section 5.6.4, this relative carbon content is an essential piece to understanding the performance difference puzzle.

The difference spectrum highlights the chromium present in the Furnace 1 sample, which may partially contribute to the enhanced performance over the Furnace 2 sample. Although Cr may exist in several oxidation states, its 3+ state is most stable, and therefore most likely in this sample – which can result in p-type doping of the Furnace 1 samples that is not occurring in the Furnace 2 samples. Further experimentation is necessary to definitively draw a conclusion for the effect of Cr on performance.

5.5 The "Mystery Sample"

The October 2008 Mystery Samples were of particular interest because of their superior performance compared to samples previously and since produced. With no intentional change in the sample preparation process, the results are to date still irreproducible. Because of the limited quantities of these samples, a high quality survey scan of the sample was measured to preserve all features for future analysis. With no immediately obvious differences between this sample and other UCSB 10 nm hematite films, another spectrum was collected on the Mystery Sample with parameters exactly matching the 10 nm December 2008 samples. A difference spectrum was then produced by subtracting the December 2008 spectrum from the Mystery sample spectrum, as shown in Figure 5.33.

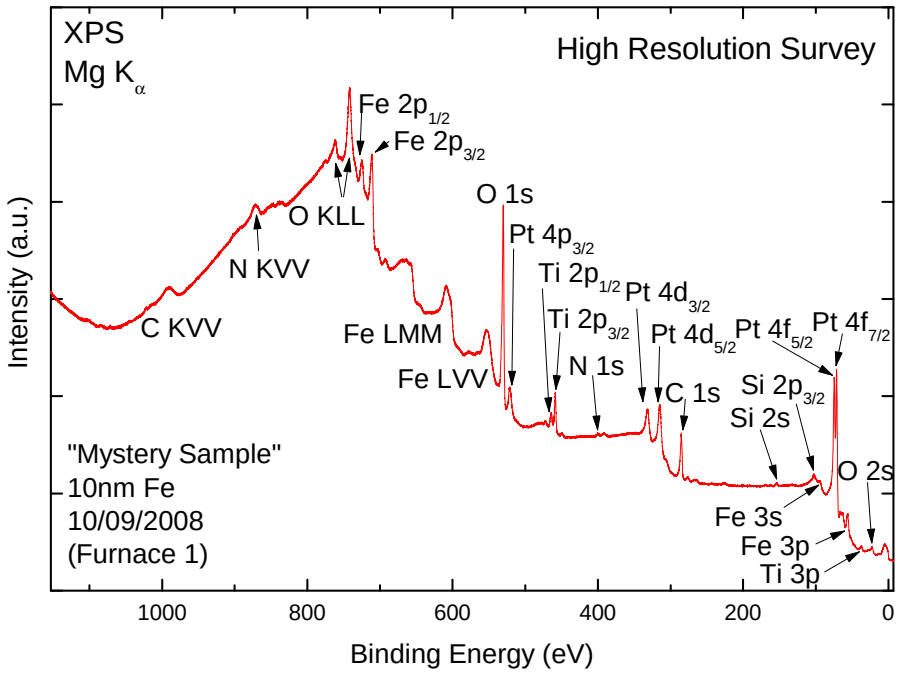

Figure 5.32: High resolution survey spectrum of 10 nm "Mystery Sample".

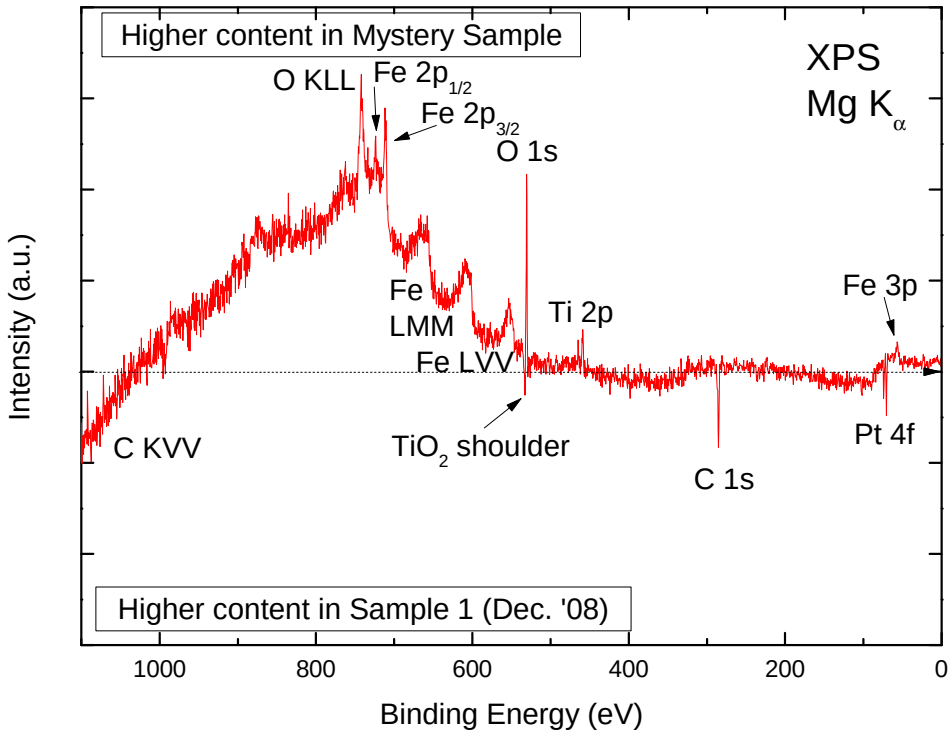

Figure 5.33: Difference spectrum of Mystery Sample and Dec. '08 10 nm Sample.

The close fit of the background to the baseline in the low binding energy region shows a good normalization fit of the two spectra. The Mystery Sample surface contains significantly less carbon than the December sample, as well as stronger O and Fe signals. The O 1s peak for Sample 1 shows a pronounced shoulder at 532.3 eV, and this feature can be seen in the difference spectrum at 532.6 eV. The Mystery Sample also shows more Pt than the December 10 nm sample, but, as will be shown in Table 5.3, the relative amount of Pt is higher in the Mystery Sample due to the significantly reduced carbon concentration. The significance of these findings will be further discussed in the subsequent "Discussion" section.

5.6 Discussion

5.6.1 Quantification of Composition

To quantify the elemental composition of the samples using our XPS data, the area under the dominant peak of each element was divided by its photoionization cross-section at 1254 eV. For this purposes, cross-sections from Scofield [28] were used, as listed in Table 5.2. Cross-sections shown are relative to C 1s. Note that these are calculated atomic cross sections, relying on a significant number of simplifications, and thus can easily deviate from the correct values by a factor of 2.

The here-computed compositions do not factor in the transmission function of the analyzer or the energy-dependence of the inelastic mean free path of the electrons. Thus, the calculations are only a rough approximation for the exact composition of each sample, while a comparative analysis across the samples, i.e., the investigation of relative changes, is more precise.

Orbital:	Fe $2p_{3/2}$	O 1s	C 1s	Pt $4f_{7/2}$	Pt $4f_{5/2}$	Ti $2p_{3/2}$
Scofield Cross Section	10.54	2.85	1.00	8.89	6.97	5.22

Table 5.2: Scofield ionization cross sections of selected elements [28]

Because of the overlap in the Pt $4f_{7/2}$ and Pt $4f_{5/2}$ peaks, the combined area under their peaks was used, and their cross-sections were summed. Table 5.3 below shows the relative content of the main elements seen in XPS. Because of its high cross-section of 7.60 (relative to the cross section of C of 1.00) and the low intensity of its $2p_{3/2}$ peak, the Cr concentration (if present) is below 0.1 % and thus not listed in Table 5.3.

Sample	Fe	O	C	Pt	Ti
Sample 1 (10 nm, Furnace 1)	3.9%	32.4%	45.8%	7.7%	10.1%
Sample 2 (200 nm Furnace 1)	28.8%	44.5%	25.6%	0.0%	1.1%
Sample 3 (400 nm Furnace 1)	17.5%	67.0%	7.3%	0.0%	8.2%
Sample 4 (200 nm Furnace 2)	7.7%	62.0%	24.7%	0.0%	5.6%
10 nm Control	4.7%	79.8%	12.2%	2.1%	1.2%
475 nm Control	22.7%	14.2%	50.4%	0.0%	12.70%
10 nm Mystery Sample	9.1%	62.4%	1.8%	14.0%	12.7%

Table 5.3: Relative Surface Composition of Samples

This composition analysis was correlated with IPCE performance data provided by UCSB. In general, a high IPCE is obtained from thin (10 and 20 nm) samples

annealed at 500°C, while intermediate thicknesses (100 nm) show much lower performance. At higher thickness (500 nm, not shown), IPCE increases again. If annealed at 700°C, the performance dip for intermediate thicknesses disappears.

Based on the Ti segregation series (Figs. 5.15-17), we can reasonably assume that the surfaces of films calcined at 500°C do not contain Ti – at least not in quantities detectable by XPS. In contrast, films calcined at 700 °C do. From the data in Table 5.3, the low Fe content of the thin 700 °C samples in fact suggests that these films might be better described as $(Fe,Ti)O_x$+Pt. Furthermore, Sample 1 and the Mystery Sample both show a higher content of Pt than Fe on the surface (the 10 nm Control sample shows a higher Fe:Pt ratio than the other samples, likely due to deposition of additional Fe during calcination, as seen in the 0 nm Control sample). We thus speculate that the titanium on the sample surfaces has a "stabilizing" effect on IPCE performance, especially in the intermediate thickness regime, where the dip in performance is much less pronounced.

The high Pt and Ti content might also help to explain the performance behavior seen in the IPCE experiments at UCSB. For example, with no applied bias, the 10 nm Sample 1 and the Mystery Sample show no photoresponse, while the thick 400 nm Sample 3 does. With an applied bias voltage of 0.4V, however, a significant IPCE response is obtained from the 10 nm Mystery Sample. With little IPCE response in an unbiased system, but a dramatic increase with applied voltage, it appears that the performance of the 10 nm Fe films is less of a photocatalytic response and more of a catalytic response, possibly due to the Pt or Ti on the sample surface. This is not to say that a photocatalytic process is completely absent, for studies have shown that

Pt-TiO_2 catalysts are not only photosensitive, but symbiotically overcome many of problems inherent in PEC oxides [29,30]. The bandgap of the Pt-doped Ti is smaller and absorbs more efficiently than that of its undoped counterpart, and the presence of Pt in the sample increases the charge-separation time – hindering recombination [29,30].

5.6.2 Oxide Formation

Figure 5.34 shows the O 1s peaks of the various calcined samples. Note that the spectral quality for Samples 2, 3, and 4 is lower than that for the other samples, since the spectra had to be taken from the survey scans.

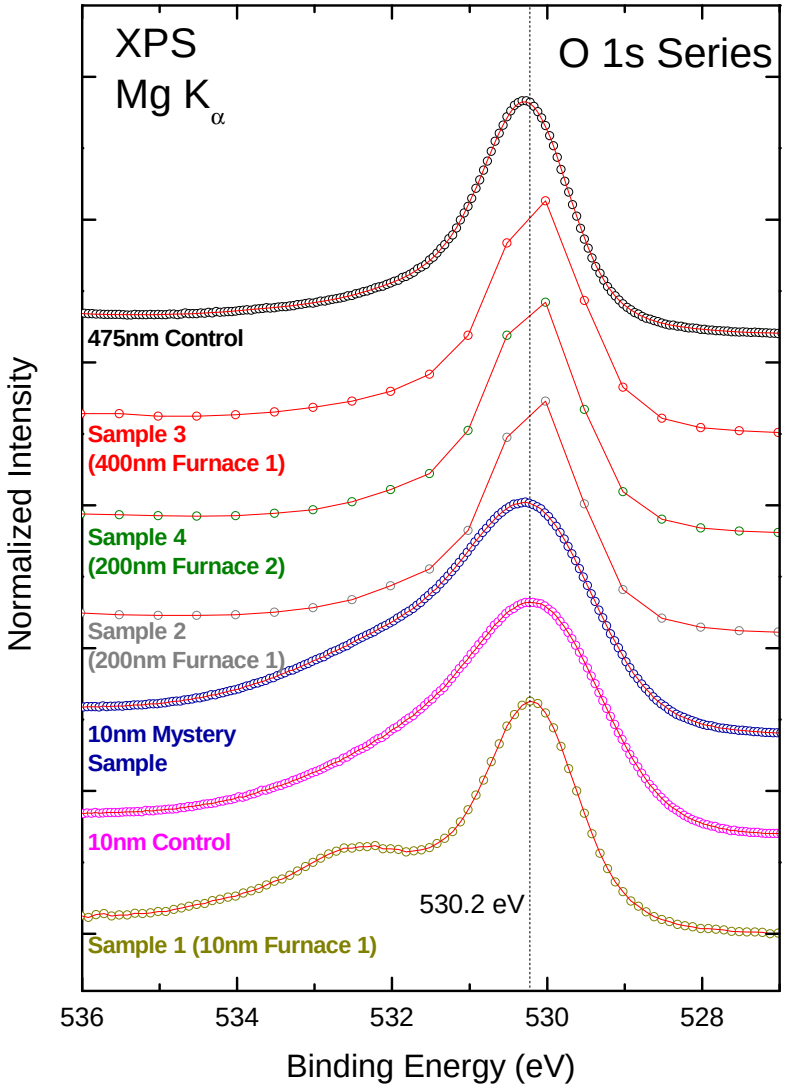

Figure 5.34: XPS spectra of the O 1s region for a variety of calcined samples.

Apart from the main oxide line at 530.2 eV, which is present for all samples, the 10 nm samples also show a distinct shoulder at higher binding energy at about 532.2 eV. This second oxide component is particularly pronounced in the 10 nm Furnace 1 sample, which, according to Table 5.3, has a particularly large Ti/Fe ratio. Furthermore, the binding energy of 532.3 eV is in close agreement with literature describing such a shoulder at 532.1 eV in TiO_2 films [31]. These findings thus also

spectroscopically suggest the presence of TiO_2 on the surface of the 10 nm samples, most clearly for the 10 nm Furnace 1 sample.

5.6.3 Film Thickness & Morphology

Apart from the variations of surface composition as a function of increasing film thickness, the morphology of the films also impact their performance. As Figure 5.19 and Figure 5.20 showed, accretion of Fe_2O_3 occurs gradually with film thickness. The pebble-like structure increases the surface area of the hematite films and increases the photoelectric performance compared to morphologies with lower surface areas. The Grätzel Group at the Ecole Polytechnique Fédérale de Lausanne have published findings that show different photoresponses for different morphologies, with high-surface-area samples outperforming their low-surface-area counterparts [32].

For this reason, the needle-like growth seen in the microscopy images may also be responsible for improving the performance of the thicker films. Several oxide studies have reported the growth of "whiskers" after metal heating, with one study showing this phenomenon appearing with Fe_2O_3 after only one minute at 700°C [33]. Voss, Butler and Mitchell have also suggested that this whisker growth occurs as hollow tubes described as "tunnels" [34]. These internal voids may help facilitate Ti diffusion through the sample from the inside of the film – explaining the detection of Ti by XPS even on the thickest Fe_2O_3 films. The Grätzel group has proposed that doping the whiskers themselves (described as nanostructures) may positively impact hematite's performance as a photoanode [35]. Doping by Ti works by

producing Fe^{2+} cations in the Fe_2O_3 lattice – creating donor sites that n-dopes the hematite material [36], and this very effect is likely taking place in the thick films.

Table 5.3 also shows an inverse relationship between film thickness and carbon content for samples prepared in the December 2008 batch. Both May 2009 control samples and the October 2008 Mystery sample do not follow this rule, however. The significance of this will be discussed in the next subsection.

5.6.4 Carbon

The surface sensitivity of the XPS technique allows us to definitively state that carbon is on the surface of the observed samples; however, experiments performed to date do not allow us to determine if this carbon is only localized on the surface, or incorporated into the sample itself. Future angle resolved experiments and gentle surface cleaning via sample warming or mild ion sputtering might be suitable to better answer this question, but for the purposes of this thesis, it is sufficient to demonstrate that the mere presence of C appears to impact the hematite film performance.

Having determined the positive effect of TiO_2 doping on the sample, an understanding of the interaction of C and TiO_2 is now necessary. Carp, Huisman, and Reller have described the deactivation of TiO_2's photosensitivity due to surface contamination by materials with higher adsorption ability – particularly identifying organics as a well-known culprit [37]. Furthermore, photonic attenuation due to carbon means that the photons seen by the photoreactive species are fewer than the total number of photons directed to the surface – negatively impacting IPCE performance.

The relatively lower carbon content of the thicker samples may explain the improvement in IPCE performance as film thicknesses increase. The source of this C contamination, however, still remains to be discussed, especially since the Mystery Sample is characterized by an extremely low carbon surface content.

Particularly puzzling is the high carbon content of the May 2009, 475 nm control sample. This sample was prepared with meticulous attention to limiting atmospheric exposure and possible contamination – yet shows higher carbon levels than samples prepared without this care. Furthermore, the 10 nm sample prepared on the same day and under the same conditions, shows a lower relative carbon content than the 10 nm sample prepared in December 2008 (as expected). A closer look at the sample preparation process may rationalize this finding.

As discussed in Chapter 4, films are prepared by electron-beam evaporation of the metals unto the substrate, forming thin layers. Pellets of the desired evaporant (metal) are placed into a graphite crucible, which is in turn placed into the e-beam evaporator (Figure 5.35).

Figure 5.35: Fe granules in new graphite crucible.


Figure 5.36: Fe-filled graphite crucible after use in the e-beam system. White arrows point at regions in the crucible wall and bottom that show damage and exposure of the crucible material (carbon).

The electron beam is rastered across the granules to prevent uneven heating and "spitting" due to hot spots; however, care has to be taken to avoid contacting the side walls of the crucible. Figure 5.36 shows an Fe-filled carbon crucible after use. White arrows point to spots of the carbon crucible that were damaged by the electron beam. It is important to note that the crucible shown in this image was used to prepare an earlier batch of Fe_2O_3 samples, but not specifically for any of the samples discussed in this thesis. For this reason, the image is illustrative only. The arrow to the lower left shows where the beam has sliced completely through the crucible, while the arrow to the right shows the beginning of this type of damage. The center arrow shows the formation of a hole due to the concentration of the electron beam within the center of the crucible. A complete burn-through of the electron beam will result in cutting through the bottom of the crucible. Crucible damage due to either cracking or burn-through will introduce carbon into the films in an uncontrolled and undesired manner.

The variability of this metal evaporation process explains why samples prepared in different batches may have such widely varying carbon content. (Even the control samples prepared on the same day have drastically different carbon content because they were prepared in two separate batches.)

Finally, the extremely low carbon content in the best performing films produced at UCSB strongly support the theory of carbon hindering Fe_2O_3 photoelectrochemical water splitting performance. Across the film thicknesses, these samples out-performed their non-Mystery counterparts, and even after one year of storage in air, the 10 nm Mystery sample had lower carbon content than any

of the samples measured shortly after synthesis. As originally suspected, the key to high-performing iron oxide PEC films may indeed lie in contamination – just not in the manner initially suspected.

CHAPTER 6

SUMMARY AND FUTURE WORK

6.1 Summary

This thesis described the characterization of α-Fe_2O_3 thin films for photoelectrochemical applications, grown by the McFarland Group at the University of California, Santa Barbara. Samples were grown by sequentially depositing 50 nm of titanium, 150 nm of platinum and varying thicknesses of iron upon a quartz substrate. These films were then annealed (calcined) under air for 4 hours at 700°C.

Secondary Ion Mass Spectroscopy (SIMS) analysis conducted by UCSB identified several contaminants, including lithium, chromium, and aluminum. UNLV's X-ray Photoelectron Spectroscopy (XPS) was able to confirm the presence of Cr in some of the samples, and rule out aluminum at the levels detectable by XPS. UNLV was unable to confirm or rule out lithium in the sample.

Scanning Electron Microscopy (SEM) images taken by UCSB showed the formation of pebble-like hematite particles that appear to grow as a function of film thickness, ranging from indistinct features in the 10 nm films, to well-formed pebbles by 200 nm films. Cross-sectional SEM images also showed the growth of needle-like whiskers growing from the sample's surface. Air Atomic Force Microscopy (AFM) imaging at UNLV also showed the emergence of islands on the surface of the films.

Before performing extensive XPS experiments at UNLV, the samples were tested to determine their durability under ionizing x-ray radiation. Beam damage tests

were performed and confirmed the durability of the sample under extended irradiation.

XPS analysis also showed titanium on the surface of samples that had been calcined. A temperature-dependent heating experiment was performed, and showed that titanium emerges through the 150 nm-thick platinum cover layer at about 700°C. Further experimentation showed that annealing a Pt-covered Ti film in air produced titanium oxide at the surface – showing that the Ti diffusion through the samples is a temperature-related phenomenon, and that the presence of TiO_2 at the surface can aid in PEC activity.

The relative composition of each PEC sample was quantified by measuring the area under dominant XPS peaks. Comparison of these data with IPCE data taken at UCSB showed that the relative carbon surface content of samples inversely impacts their photocatalytic response, with higher carbon levels lowering the IPCE performance. This thesis proposes that the carbon contamination in the samples stems from the graphite crucibles used during the film deposition process, thus suggesting an explanation for the origin of superior "mystery" performance of samples with unusually low carbon levels at the surface.

6.2 Future Work

The characterization work covered in this thesis focused exclusively on the physical properties of the α-Fe_2O_3 films, but the electronic structure of photoelectrochemical materials is equally important to understanding, modeling and predicting their behavior. The Heske Group at UNLV has previously produced an all-experimental picture of the electronic properties at a WO_3 thin film surface –

disproving several basic assumptions about the material in the process. Such a picture of Fe_2O_3 would be valuable in determining its true viability as a PEC material.

Experiments of this nature require the least-contaminated samples possible, for even trace amounts of contamination can dope the samples and impact their band structures. Such a prototypical α-Fe_2O_3 sample can be prepared by introducing a high purity iron foil into our ultra-high vacuum (UHV) system. This sample can then be annealed at high temperature under high purity O_2 to form Fe_2O_3 (using a very recently completed oxygen annealing chamber connected to the UHV system). This approach would circumvent the need for the titanium binding layer and minimize Ti contamination due to diffusion through the system.

The crystal structure of the iron oxide surface can be evaluated within the UHV system by Low Energy Electron Diffraction (LEED), and then transferred to the Analysis Chamber for XPS analysis to confirm the sample purity. Ultraviolet Photoelectron Spectroscopy (UPS) within this same chamber can experimentally determine the valence band edge of the sample, while Inverse Photoemission (IPES) can determine the conduction band edge – thus, in total experimentally determining the Fe_2O_3 band gap, band edge positions, and work function at the surface.

More long-term planned experimentation involves the in-situ analysis of Fe_2O_3; under PEC-like conditions in electrolyte. The Heske group currently has capabilities at Beamline 8.0 at the Berkeley Lab's Advanced Light Source to analyze liquids using soft x-ray photon-in-photon-out spectroscopy– a crucial first step towards this. Such an experiment will provide insights into the chemistry of the material during

the photoelectrochemical process, in particular in view of photochemical degradation.

BIBLIOGRAPHY

[1] Gueymard, C.A.; The sun's total and spectral irradiance for solar energy applications and solar radiation models. *Solar Energy* **2004**, *76*, 423–453.

[2] Stickler, G.; Kyle, L.; *Solar Radiation and the Earth System* http://edmall.gsfc.nasa.gov/inv99Project.Site/Pages/science-briefs/ed-stickler/ed-irradiance.html (accessed October 2, 2009). National Aeronautics and Space Administration (NASA).

[3] International standard ISO 9845-1, 1992. http://pvcdrom.pveducation.org/APPEND/Am1_5.htm (accessed October 2, 2009). Photovoltaic Education Network, ASTM G-173-03.

[4] United States Committee on Extension to the Standard Atmosphere, "U.S. Standard Atmosphere, 1976", National Oceanic and Atmospheric Administration, National Aeronautics and Space Administration, United States Air Force, Washington D.C., 1976.

[5] Barbir, F.; PEM electrolysis for production of hydrogen from renewable energy sources. *Solar Energy* **2005,** *78*, 661–669.

[6] World Energy Council. *Fuel Cell efficiency*. 7/17/2007. http://www.worldenergy.org/focus/fuel_cells/377.asp. (accessed 11/15/2009).

[7] U.S. Department of Energy, U.S. Environmental Agency. *Advanced Technologies & Energy Efficiency.* http://www.fueleconomy.gov/feg/atv.shtml (accessed October 7, 2009).

[8] Honda FCX Clarity – Fuel Cell Comparison. http://automobiles.honda.com/fcx-clarity/fuel-cell-comparison.aspx (accessed 11/16/2009).

[9] IGCC, Supercritical. http://www.worldcoal.org/coal-the-environment/coal-use-the-environment/improving-efficiencies/ (accessed 11/16/2009). World Coal Institute.

[10] Fujishima, A.; Honda, K.; Electrochemical Photolysis of Water at a Semiconductor Electrode. *Nature* **1972,** *238,* 37-38.

[11] Ulleberg, Ø.; Modeling of advanced alkaline electrolyzers: a system simulation approach. *Int. J. Hydrogen Energy* **2003,** *28*, 21-33.

[12] Turner, J.; Deutsch, T.; Leisch, J.; Wang, H.; Photoelectrochemical Systems for H_2 Production. *DOE Hydrogen Program FY 2005 Progress Report.*

[13] Bak, T.; Nowotny, J.; Rekas, M., Sorrell, C.C.; Photo-electrochemical hydrogen generation from water using solar energy. Materials-related aspects. *Int. J. Hydrogen Energy* **2002**, *27*, 991-1022.

[14] Kormann, C.; Bahnemann, D.W.; Hoffmann, M.R.; Environmental Photochemistry: Is Iron Oxide (Hematite) an Active Photocatalyst? A Comparative Study: α-Fe_2O_3, ZnO, TiO_2. *J. Photochem. Photobiol., A* **1989**, *4*, 161-169.

[15] Huda, M.; Walsh, A.; Wei, S-H.; Yan, Y.; Al-Jassim, M.; Turner, J.; Theory of Oxides for Photoelectrochemical Hydrogen Production. **[Online] 2008** http://www.hydrogen.energy.gov/pdfs/review08/pdp_34_turner.pdf (accessed May 2, 2009).

[16] Cesar, I.; Kay, A.; Martinez, Jos A.; Grätzel, M.; Translucent Thin Film Fe_2O_3 Photoanodes for Efficient Water Splitting by Sunlight: Nanostructure-Directing Effect of Si-Doping. *J. Am. Chem. Soc.* **2006**, *128*, 14.

[17] Iordanova, N.; Dupuis, M.; Rosso, K.M.; Charge transport in metal oxides: A theoretical study of hematite α-Fe_2O_3. *J. of Chem. Phys*. **2005**, *122*, 144305.

[18] Hertz, H.; Über sehr schnelle elektrische Schwingungen, *Ann. Physik* **1887,** *31*, 421.

[19] Hallwachs, W.; Über den Einfluβ des Lichtes auf elektrostatisch geladene Körper, *Ann. Physik* **1888**, 33, 301.

[20] Briggs, D.; Seah, M.P.; *Practical Surface Analysis*, John Wiley & Sons Ltd., Chicheser, England (1990).

[21] Atkins, P.; de Paula, J.; *Atkins' Physical Chemistry, Seventh Edition*, Oxford University Press, Oxford, England (2002).

[22] Grimes, C.A.; Varghese, O.K.; Ranjan, S.; *Light, Water, Hydrogen. Solar Generation of Hydrogen by Water Photoelectrolysis*. Springer Science+Business Media, LLC., New York City, NY USA (2007).

[23] *Measurements of PEC hydrogen production materials*, (2009), http://www2.eere.energy.gov/hydrogenandfuelcells/pec_standards_review.html. (accessed November 13, 2009). U.S. Department of Energy.

[24] Park Systems. *Park Systems New XE-70 AFM/SPM with Decoupled XY and Z Scanners Eliminates Artifacts from Cross-Talk in Images*, 2007, http://www.nanotech-now.com/news.cgi?story_id=22812 (accessed November 13, 2009).

[25] Moulder, J. F.; Stickle, W. F.; Sobol, P. E.; Bomben, K. D.; *Handbook of X Ray Photoelectron Spectroscopy: A Reference Book of Standard Spectra for Identification and Interpretation of XPS Data*; Physical Electronics, 1995.

[26] Park, R. L.; Lagally, M. G.; *Solid State Physics: surfaces*. Academic Press, Orlando, FL USA (1985).

[27] Weinhardt, L.; Blum, M.; Bär, M; and Heske, C.; Electronic surface level positions of WO_3 thin films for photoelectrochemical hydrogen production. *J. Phys. Chem. C,* **2008,** *112,* 3078-3082.

[28] Scofield, J.H.; Hartree-Slater Subshell Photoionization Cross-sections at 1254 and 1487 eV. *J. Electron. Spectrosc. Relat. Phenom.* **1976**, *8*, 129-137.

[29] Li, F.B.; Li, X.Z.; The Enhancement of photodegradation efficiency using Pt-TiO_2 catalyst. *Chemosphere* **2002**, *48*, 1103-1111.

[30] Hu, Y-S.; Kleiman-Shwarsctein, A.; Forman, A.J.; Hazen, D.; Park, J-N.; McFarland, E.W. Pt-Doped α-Fe2O3 Thin Films Active for Photoelectrochemical Water Splitting. *Chem. Mater.* **2008**, *20*, 3803-3805.

[31] Stefanov, P.; Shipochka, M.; Stefchev, P.; Raicheva, Z.; Lasarova, V.; Spassov, L.; XPS characterization of TiO_2 layers deposited on quartz plates. *J. of Phys.: Conference Series 100* **2008**, 012039.

[32] Cesar, I.; Kay, A.; Gonzalez Martinez, J.; Grätzel, M.; Translucent Thin Film Fe2O3 Photoanodes for Efficient Water Splitting by Sunlight: Nanostructure-Directing Effect of Si-Doping. *J. Am. Chem. Soc*. **2006**, *128*, 4582-4583.

[33] Takagi, R.; Growth of Oxide Whiskers on Metals at High Temperature. *J. Phys. Soc. Jpn.* **1957**, *12 (11)*, 1212-1218.

[34] Voss, D.A.; Butler, E.P.; Mitchell, T.E.; The Growth of Hematite Blades during the High Temperature Oxidation of Iron. *Metall. Trans. A* **1982**, *13A*, 929-935.

[35] Kay, A.; Cesar, I.; Grätzel, M.; New Benchmark for Water Photooxidation by Nanostructured α-Fe2O3 Films. *J. Am. Chem. Soc.* **2006**, *128 (49),* 15714-15721.

[36] Morin, F. J.; Electrical Properties of αFe_2O_3 and αFe_2O_3 Containing Titanium. Phys. Rev. **1951**, *83 (5)*, 1005-1011.

[37] Carp, O.; Huisman, C.L.; Reller, A.; Photoinduced reactivity of titanium dioxide. Prog. Solid State Chem. **2004**, *32*, 33-177.

VITA

Graduate College
University of Nevada, Las Vegas

Kyle E. N. George

Degrees:

Bachelor of Arts, Chemistry, 2008
University of Nevada, Las Vegas

Special Honors and Awards:

Vice President – UNLV Graduate & Professional Student Association (GPSA)
Chair, UNLV GPSA Grants Committee
Chair, UNLV GPSA Research Forum Committee
Chair, UNLV GPSA Government Relations Ad-hoc Committee
Chair, UNLV GPSA Budget Crisis Ad-hoc Committee
Chemistry Representative – UNLV College of Sciences Graduate Council
2008 UNLV Undergraduate Commencement Speaker
2008 UNLV Distinguished Graduate
2nd Place – Tri-State 2008 Reynolds Governor's Cup
1st Place – Nevada State 2008 Reynolds Governor's Cup
Chair – UNLV College of Sciences Undergraduate Council
Member – Golden Key International Honour Society
Recipient – Carter G. Woodson Scholarship (UNLV)
Recipient – Renee & Martin Paluga Scholarship (UNLV)

Publications:

"Impact of air-exposure on the chemical and electronic structure of ZnO:Zn_3N_2 thin films",
M. Bär, K.-S. Ahn, Y. Yan, L. Weinhardt, O. Fuchs, M. Blum, **K. George**, S. Pookpanratana, W. Yang, J.D. Denlinger, M. Al-Jassim, and C. Heske, Appl. Phys. Lett. 94, 012110 (2009). (3 pages)

Thesis Title: Characterization of Fe_2O_3 Thin Films for Photoelectrochemical Hydrogen Production

Thesis Examination Committee:

Chairperson, Clemens Heske, Dr. rer. nat.
Committee Member, David Hatchett, Ph.D.
Committee Member, Dong-Chan Lee, Ph.D.
Graduate Faculty Representative, James Selser, Ph.D.